NASA TECHNICAL NOTE

NASA TN D-6054

NASA TN D-6054

STRESS INTENSITY MAGNIFICATION FOR DEEP SURFACE CRACKS IN SHEETS AND PLATES

by Robert B. Anderson, Arthur G. Holms, and Thomas W. Orange

Lewis Research Center
Cleveland, Ohio 44135

NATIONAL AERONAUTICS AND SPACE ADMINISTRATION • WASHINGTON, D. C. • OCTOBER 1970

DISCLAIMER NOTICE

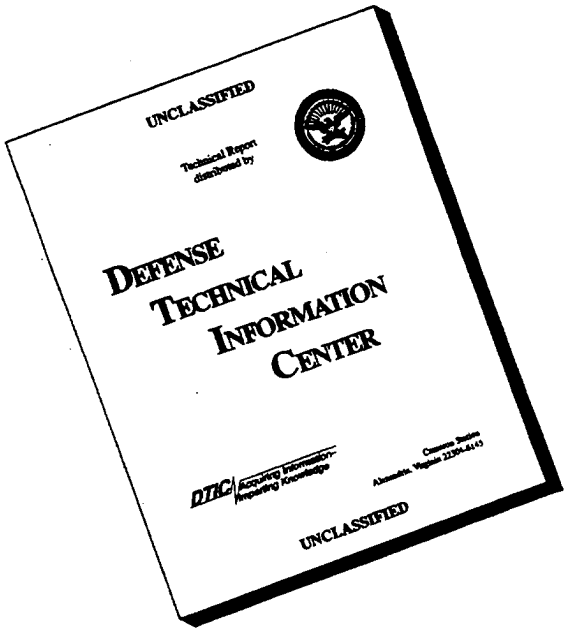

THIS DOCUMENT IS BEST QUALITY AVAILABLE. THE COPY FURNISHED TO DTIC CONTAINED A SIGNIFICANT NUMBER OF PAGES WHICH DO NOT REPRODUCE LEGIBLY.

1. Report No. NASA TN D-6054	2. Government Accession No.	3. Recipient's Catalog No.
4. Title and Subtitle STRESS INTENSITY MAGNIFICATION FOR DEEP SURFACE CRACKS IN SHEETS AND PLATES		5. Report Date October 1970 6. Performing Organization Code
7. Author(s) Robert B. Anderson, Arthur G. Holms, and Thomas W. Orange		8. Performing Organization Report No. E-5708
9. Performing Organization Name and Address Lewis Research Center National Aeronautics and Space Administration Cleveland, Ohio 44135		10. Work Unit No. 124-08 11. Contract or Grant No. 13. Type of Report and Period Covered Technical Note
12. Sponsoring Agency Name and Address National Aeronautics and Space Administration Washington, D.C. 20546		14. Sponsoring Agency Code

15. Supplementary Notes

16. Abstract

The Irwin stress intensity factor for surface cracks with crack depths less than half the plate thickness is extended to cases of relatively deep cracks by including the effect of the free surface opposite the crack. The stress intensity magnification factor is given as a function of applied load, crack length, crack depth, sheet thickness, yield strength, and Poisson's ratio. The combinations of these variables for which the plastic zone extends completely through the thickness are also predicted. The range of applicability of the analysis to surface-crack specimen data was investigated in terms of crack-depth-to-specimen-thickness ratio and crack depth-to-length ratio.

17. Key Words (Suggested by Author(s))	18. Distribution Statement
Crack propagation; Fracture mechanics; Fracture strength; Notch tests; Surface cracks; Toughness; Stress intensity factor; Surface crack specimens; Deep surface cracks; Stress intensity magnification; and Crack tip plasticity.	Unclassified - unlimited

19. Security Classif. (of this report)	20. Security Classif. (of this page)	21. No. of Pages	22. Price*
Unclassified	Unclassified	53	$3.00

*For sale by the Clearinghouse for Federal Scientific and Technical Information
Springfield, Virginia 22151

CONTENTS

STRESS INTENSITY MAGNIFICATION FOR DEEP SURFACE CRACKS IN SHEETS AND PLATES

by Robert B. Anderson*, Arthur G. Holms, and Thomas W. Orange

Lewis Research Center

SUMMARY

The Irwin stress intensity factor for surface cracks with crack depths less than half the plate thickness is extended to cases of relatively deep cracks by including the effect of the free surface opposite the crack. The resulting stress intensity magnification factor is expressed as a function of applied load, crack length, crack depth, sheet thickness, yield strength, and Poisson's ratio. In addition, a method is proposed for predicting those combinations of load, geometry, and material properties for which the plastic zone would extend completely through the thickness. Such conditions are regarded as limiting on the validity of the analysis.

The proposed analysis was applied to some published surface-crack data for specimens made from an epoxy, from an aluminum alloy, and from a titanium alloy. The metals had been tested in environments of liquid nitrogen and liquid hydrogen. The modified critical stress intensity factor was found to remain essentially constant (within ±10 percent) for wide variations of the crack depth-to-length ratio and for wide variations in the crack-depth-to-specimen-thickness ratio.

INTRODUCTION

The need for minimum-weight flight tankage for aerospace applications has brought increasing concern about failure of such vessels at pressures below the operating level. The use of high-strength materials and failure criteria based on yield or ultimate strength can give erroneously high computed margins of safety against failure. Many instances of unexpected failures have been documented wherein brittle-mode fractures were traceable to a small crack or defect that was not detected by available methods of nondestructive flaw inspection. Such brittle failures can often occur at nominal stresses well below the yield strength of the material.

*Presently affiliated with Carnegie-Mellon University, Pittsburgh, Pa.

Designing against brittle-mode failures requires that the designer be able to assess the crack resistance of candidate materials, and that he be able to predict the effect of crack size and shape on structural strength. Such predictions can best be made if a convenient mathematical model of the defect is available. Many surface cracks and embedded flaws have been observed which can reasonably be approximated by semielliptical and elliptical shapes, respectively.

G. R. Irwin (ref. 1) derived an expression for the stress intensity around an elliptical crack in an infinite elastic solid under tension and a correction for the effect of small-scale yielding at the crack tip. He also estimated the effect of the two free surfaces that are present in a finite-thickness plate containing a semielliptical surface crack. His analysis is thought to be reasonably accurate when the crack depth is less than half the plate thickness and when yielding is restricted to a small zone at the crack tip.

For thin-walled pressure vessels, the largest nondetectable flaw might not be small compared to the wall thickness, and the free-surface correction factor of reference 1 might not be adequate as is evidenced by the decrease of computed fracture toughness with increasing crack-depth-to-specimen-thickness ratio a/t (ref. 2). In order to extend the shallow-crack analysis to deep cracks, the effect of the back (uncracked) surface on the stress intensity and also on the plastic-zone size at the crack tip must be determined. The critical stress intensity is anticipated to be a materials constant (plane-strain fracture toughness) as long as the deformation at the crack tip is highly constrained. If the crack tip is not remote from the stress-free back surface, the constraint is lacking and the computed fracture toughness may be geometry-dependent. For this reason, a deep-flaw analysis should describe the conditions under which the assumption of a plane-strain fracture toughness might not be applicable.

Such an analysis can have two applications. First, for materials evaluation, one must know the ranges of specimen geometry and material conditions that will permit a valid analysis and, thereby, a useful measurement of fracture toughness. Secondly, the structural designer can predict fracture load for a given flaw geometry when the material's fracture toughness is known. In either case, one must know the range of flaw geometry for which the analysis is usable.

An exact and complete treatment of the problem would require the solution of a three-dimensional elastic-plastic boundary value problem. Until such a solution is available in useful form, reasonable approximations based on available elastic solutions might be used to develop an expression that accounts for finite thickness and crack-tip plasticity in rather simple form. One such effort is mentioned in reference 2, and another (which contains an indeterminate quantity that might be approximated by the ultimate tensile strength) is described in reference 3.

In the present report, Irwin's analysis is modified to reflect the effects of the stress-free plate surfaces and the crack-tip plastic zone. The resulting stress

intensity magnification factor is given as a function of crack depth and length, plate thickness, applied stress, yield strength, and Poisson's ratio. A method is proposed for estimating the conditions under which the plastic zone would extend completely through the thickness (this being considered an upper limit on the validity of the analysis). This analysis and those of references 1 and 3 are applied to several sets of deep-flaw data from the literature. The results of the three analyses are compared as joint functions of the crack-depth-to-plate-thickness ratio and the crack depth-to-length ratio, over the ranges of some published data.

ANALYSIS FOR LONG INTERNAL CRACKS

The stress intensity factor derived by Irwin in reference 1 applies to elliptical cracks in plates in which the ratios of crack depth to plate thickness and crack length to plate width are small. In the present analysis, a magnification factor is developed to account for the effects of finite plate thickness and crack-tip plasticity. The magnification factor is an approximation based on a crack-tip stress analysis and a plastic-zone analysis for plates having coplanar through-cracks.

Irwin Stress Intensity Factor

The opening-mode stress intensity factor along the boundary of an internal elliptical flat crack in a body subjected to remote uniform tensile stress σ normal to the plane of the crack is given by Irwin (ref. 1) as

$$K_I(\varphi) = \frac{\sigma}{\Phi}\sqrt{\frac{\pi a}{c}}\left(a^2 \cos^2\varphi + c^2 \sin^2\varphi\right)^{1/4} \tag{1a}$$

where

$$\Phi = \int_0^{\pi/2} \left(\sin^2\varphi + \frac{a^2}{c^2}\cos^2\varphi\right)^{1/2} d\varphi \tag{1b}$$

and φ is defined by $x = a \sin\varphi$, $z = c \cos\varphi$ for a crack oriented and dimensioned as in figure 1. (All symbols are defined in appendix F.)

With $c > a$, the stress intensity is largest at a value of φ equal to $\pi/2$, which occurs at $x = \pm a$ and $z = 0$, the points of intersection of the ellipse with its minor

axis. The maximum stress intensity factor on the elliptical boundary, hereinafter denoted simply by K_I, is

$$K_I = \frac{\sigma\sqrt{\pi a}}{\Phi} \tag{2}$$

As defined in equation (1b), Φ is a function of the ratio of the axes of the ellipse a/c. For long cracks for which a/c approaches zero, Φ approaches 1 and the stress intensity factor is

$$K_I = \sigma\sqrt{\pi a} \tag{3}$$

In reference 1, the effect of plastic deformation at the crack tip is accounted for by augmenting the depth of the crack by $K_I^2/(4\pi\sqrt{2}\,Y^2)$, a term derived from the assumption of plane strain near the crack tip, in which Y is the uniaxial yield strength. With this correction, equation (2) becomes

$$K_I = \sigma\sqrt{\frac{\pi a}{\Phi^2 - 0.177\left(\frac{\sigma}{Y}\right)^2}} \tag{4}$$

Effect of Sheet Thickness

In this analysis, the three-dimensional problem of deep elliptical cracks is approximated as a plane problem in which the crack border near the minor elliptical axis is assumed to be straight. Accordingly the magnification factor developed in this section is intended to apply to elliptical cracks for which the depth-to-length ratio is small. It is further assumed that the magnification of the stress intensity near the minor axis of a long, elliptical, internal crack in a plate of finite thickness, as shown in figure 2(a), can be approximated by that for a through-crack that is one of a series of coplanar cracks in a plate, as shown in figure 2(c).

The opening-mode stress intensity factor for the latter case was given in reference 4 and is derived in reference 5 (p. 35) from the Westergaard stress function for coplanar cracks. It is expressed by

$$K_I = \sigma\sqrt{\pi b}\; f\left(\frac{b}{W}\right) \tag{5}$$

in which b is half the length of the through-crack, W is the spacing of the coplanar cracks, and

$$f\left(\frac{b}{W}\right) = \sqrt{\frac{W}{\pi b} \tan \frac{\pi b}{W}} \tag{6}$$

It can be seen in equation (6) that f(b/W) reduces to unity for small b/W, in which case equation (5) becomes

$$K_I = \sigma \sqrt{\pi b} \tag{7}$$

Hence the function f(b/W) can be viewed as a magnification factor multiplying the stress intensity factor for an isolated crack. It is now assumed that a similar magnification factor of the form f(a/t) for a long, internal crack of depth 2a in a plate of thickness t can be applied to the stress intensity factor in equation (3). The magnified stress intensity factor is then

$$K_I = \sigma \sqrt{\pi a}\, f\left(\frac{a}{t}\right) \tag{8}$$

in which

$$f\left(\frac{a}{t}\right) = \sqrt{\frac{t}{\pi a} \tan \frac{\pi a}{t}} \tag{9}$$

The correction function of equation (9) was proposed in reference 5, in which the accuracy of the thickness correction was stated to be doubtful (p. 51) if the crack-tip plasticity subtends a major portion of the distance from the crack tip to the back face of the plate. The correction function (eq. (9)) should therefore be altered to include the effect of crack-tip plasticity and should reflect the dependence of the plastic enclave size on plate thickness, crack shape, and applied load.

Effect of Crack-Tip Plasticity

If yielding occurs at the tip of the crack and extends a distance ahead of the crack, a fraction of this distance should be added to the actual crack length in the stress intensity expression to account for effects of the yielded zone, as discussed in reference 6. Consequently, the crack dimension a in equations (8) and (9) is replaced by $a + \lambda R$, in

which λR is a fraction of the length R of the plastic zone. The stress intensity factor for a long internal flaw thus corrected is

$$K_I = \sigma\sqrt{t \tan\left[\frac{\pi a}{t}\left(1 + \lambda \frac{R}{a}\right)\right]} \tag{10}$$

In reference 1, Irwin proposed that the plastic-zone correction factor $1 + \lambda(R/a)$ be equal to $1 + K_I^2/a(4\pi\sqrt{2}\,Y^2)$ as long as the ratio of applied stress to yield strength σ/Y is sufficiently small. For σ/Y or a/t not sufficiently small, this correction factor may underestimate the extent of crack-tip plasticity. In appendix A of this report, the plastic-zone correction factor is derived for a plate cut by a series of coplanar cracks. When applied to the plastic zone near the minor axis of a long internal elliptical crack in a plate of thickness t, the correction factor analogous to that of equation (A6) becomes

$$1 + \lambda \frac{R}{a} = \frac{t}{\pi a} \arcsin\left[\sqrt{1 - \left(\frac{\sigma}{\sigma_Y}\right)^2}\, \sin \frac{\pi a\left(1 + \frac{R}{a}\right)}{t}\right] \tag{11}$$

In equation (11), σ_Y is the tensile stress normal to the plane of the crack at the elastic-plastic interface. The length R of the zone of plasticity ahead of a crack in a plate that contains a series of coplanar cracks is derived in reference 7 and rederived in appendix B. This plastic-zone analysis relates R to the crack spacing W, applied stress σ, and crack length 2b by

$$R = \frac{W}{\pi} \arcsin\left[\left(\sin \frac{\pi b}{W}\right)\left(\sec \frac{\pi \sigma}{2\sigma_Y}\right)\right] - b \tag{12}$$

It is now proposed that an analogous expression be used to estimate the size of the plastic enclave in front of a long internal crack of depth 2a in a plate of thickness t. In the analogous expression, the through-crack length 2b would be replaced by the corresponding internal crack dimension 2a, and the dimension W replaced by the thickness t. The resulting expression for the length of the plastic enclave at the root of the internal flaw is

$$R = \frac{t}{\pi} \arcsin\left[\left(\sin \frac{\pi a}{t}\right)\left(\sec \frac{\pi \sigma}{2\sigma_Y}\right)\right] - a \tag{13}$$

Insertion of the plastic enclave length of equation (13) into equation (11) results in the following expression for the plastic-zone correction factor:

$$1 + \lambda \frac{R}{a} = \frac{t}{\pi a} \arcsin\left[\sqrt{1 - \left(\frac{\sigma}{\sigma_Y}\right)^2} \sin\frac{\pi a}{t} \sec\frac{\pi\sigma}{2\sigma_Y}\right] \tag{14}$$

The stress at the elastic-plastic interface, appearing as σ_Y in equations (11) to (14), is very sensitive to the degree of constraint at the crack tip. Certainly in the case of surface cracks and internal cracks, plastic deformation at the crack tip is highly constrained and σ_Y is larger than the uniaxial yield strength. Exactly how much larger is difficult to assess because the degree of constraint depends on the size of the plastic enclave and the distance from the crack tip to the stress-free surface. If this distance is large relative to the plastic enclave length (fig. 3), enough constraint is provided by surrounding elastic material to increase σ_Y to perhaps several times the uniaxial yield strength. If, however, plasticity spreads from the crack tip to the free surface, there is little constraint and σ_Y may be only slightly larger than the uniaxial yield strength. Specific values of σ_Y can be derived from the examination of the stress state at the elastic-plastic interface.

State of Stress at Elastic-Plastic Interface

Consider that the plastic enclave has spread to a length R in front of a flat surface crack in a plate, as shown in figure 3. Of particular interest is the point (a + R, 0, 0) on the elastic-plastic boundary nearest the uncracked stress-free surface. The elastic strain component ϵ_Z at this point is related to the stress components by

$$\epsilon_Z = \frac{1}{E}(\sigma_Z - \nu\sigma_Y - \nu\sigma_X) \tag{15}$$

in which E is Young's modulus and ν is Poisson's ratio.

In the case of a long internal crack, the radius of curvature of the crack front is large near the point (a + R, 0, 0). Hence, the problem can be represented as a plane problem; and, if the plastic enclave depth is small relative to the crack depth, the deformation condition in the region near the point (a + R, 0, 0) is reasonably approximated by plane strain. In this case

$$\sigma_Z = \nu(\sigma_X + \sigma_Y) \tag{16}$$

The Von Mises condition for yielding requires that

$$(\sigma_X - \sigma_Y)^2 + (\sigma_Y - \sigma_Z)^2 + (\sigma_X - \sigma_Z)^2 + 6(\tau_{XY}^2 + \tau_{YZ}^2 + \tau_{XZ}^2) = 2Y^2 \tag{17}$$

At the point $(a + R, 0, 0)$, the shear stress components τ_{YX}, τ_{YZ}, and τ_{XZ} are zero because of symmetry; and the yield condition reduces to

$$(\sigma_X - \sigma_Y)^2 + (\sigma_Y - \sigma_Z)^2 + (\sigma_X - \sigma_Z)^2 = 2Y^2 \tag{18}$$

The ratio σ_Y/Y is obtained from the solution of equations (16) and (18), as

$$\frac{\sigma_Y}{Y} = \left[(1 - \nu + \nu^2)\left(1 + \frac{\sigma_X}{\sigma_Y}\right)^2 - 3\frac{\sigma_X}{\sigma_Y}\right]^{-1/2} \tag{19}$$

Thus the ratio σ_Y/Y is a function of ν and the ratio σ_X/σ_Y. The latter ratio is highly dependent on the size of the plastic enclave and on the proximity of the leading edge of the plastic zone to the opposite free surface of the plate.

To determine σ_Y/Y accurately for the general case would require the solution of a three-dimensional elastic-plastic boundary value problem. In the present analysis, the ratio σ_X/σ_Y for a long internal crack is assumed to be the same as that for one of a series of coplanar through-cracks, as derived in appendix C. When referred to a long internal crack of depth $2a$ in a plate of thickness t, the relation corresponding to equation (C7) in appendix C is

$$\frac{\sigma_X}{\sigma_Y} = 1 - \frac{\dfrac{\sigma}{\sigma_Y}}{\left\{1 - \left[1 - \left(\dfrac{\sigma}{\sigma_Y}\right)^2\right]\sin^2\left(\dfrac{\pi a}{t}\right)\sec^2\left(\dfrac{\pi\sigma}{2\sigma_Y}\right)\right\}^{1/2}} \tag{20}$$

Solution of equations (13), (19), and (20) for the special case of a highly constrained plastic zone (R approaches zero) results in

$$\frac{\sigma_Y}{Y} = \frac{1}{1 - 2\nu} \tag{21}$$

and for the case in which the plastic zone reaches the surface ($\sigma_X = 0$),

$$\frac{\sigma_Y}{Y} = \frac{1}{\sqrt{1 - \nu + \nu^2}} \tag{22}$$

Magnification Factor for Long Internal Cracks

The stress intensity factor for a long internal flaw uncorrected for either plasticity or thickness effects is given as $\sigma\sqrt{\pi a}$ in equation (3). The ratio of the corrected stress intensity factor to the uncorrected stress intensity is found by dividing equation (10) by $\sigma\sqrt{\pi a}$. A similarly defined ratio is referred to in reference 2 as the magnification factor. In the present work this ratio for long internal cracks is

$$M_i = \left\{\frac{t}{\pi a} \tan\left[\frac{\pi a}{t}\left(1 + \lambda \frac{R}{a}\right)\right]\right\}^{1/2} \tag{23}$$

Solution of equations (14), (19), (20), and (23) would give M_i as a function of a/t, σ/Y, and ν.

APPLICATION TO DEEP SURFACE CRACKS

In references 1 and 5 the stress intensity factor for internal elliptical cracks in infinitely thick plates (eq. (2)) is modified to apply to semielliptical surface cracks by use of a correction factor that accounts for the effect of the cracked, stress-free face of the plate. The resulting stress intensity factor for surface cracks, modified to reflect crack shape effects but uncorrected for crack-tip plasticity or plate thickness, is given in reference 5 as

$$K_{I0} = \left[1 + 0.12\left(1 - \frac{a}{c}\right)\right]\sigma\sqrt{\pi a^*} \tag{24}$$

in which

$$a^* = \frac{a}{\Phi^2} \tag{25}$$

and the bracketed term in equation (24) represents the correction for the effect of the stress-free cracked surface of the plate, and the term Φ^2 in equation (25) reflects the effect of crack shape.

In the previous section, a magnification factor for long internal cracks was developed (eq. (23)) that incorporates the influences of plasticity and plate thickness. It is now suggested that this magnification factor, used with the corrections of equations (24) and (25), could represent the magnification effect for deep surface cracks. As an approximation to the influence of crack shape on the magnification, it is proposed that the term a^* that appears in equation (24) be used in place of the crack depth a and that the surface-crack depth-to-thickness ratio a/t replace the internal-crack depth-to-thickness ratio $2a/t$ in equations (13), (14), (20), and (23). Accordingly, equation (20) becomes

$$\frac{\sigma_X}{\sigma_Y} = 1 - \frac{\sigma}{\sigma_Y}\left\{1 - \left[1 - \left(\frac{\sigma}{\sigma_Y}\right)^2\right]\sin^2\left(\frac{\pi a^*}{2t}\right)\sec^2\left(\frac{\pi\sigma}{2\sigma_Y}\right)\right\}^{-1/2} \tag{26}$$

The plastic-zone correction factor in equation (14) is now

$$1 + \lambda\frac{R}{a^*} = \frac{2t}{\pi a^*}\arcsin\left\{\left[1 - \left(\frac{\sigma}{Y}\right)^2\left(\frac{Y}{\sigma_Y}\right)^2\right]^{1/2}\left[\sin\left(\frac{\pi}{2}\frac{a^*}{t}\right)\right]\left[\sec\left(\frac{\pi}{2}\frac{\sigma}{Y}\frac{Y}{\sigma_Y}\right)\right]\right\} \tag{27}$$

The length of the plastic zone from equation (13) becomes

$$R = \frac{2t}{\pi}\arcsin\left\{\left[\sin\left(\frac{\pi a^*}{2t}\right)\right]\left[\sec\left(\frac{\pi}{2}\frac{\sigma}{\sigma_Y}\right)\right]\right\} - a^* \tag{28}$$

Using the front surface correction of equation (24) and the thickness correction of equation (23), the stress intensity factor is written

$$K_I = \sigma\sqrt{\pi a^*}\,M \tag{29}$$

where from comparison with equations (23) and (24),

$$M = \left[1 + 0.12\left(1 - \frac{a}{c}\right)\right]\left\{\frac{2t}{\pi a^*}\tan\left[\frac{\pi a^*}{2t}\left(1 + \lambda\frac{R}{a^*}\right)\right]\right\}^{1/2} \tag{30}$$

The development of equation (30) assumes no interaction between the stress-free front and back surfaces.

Solution of equations (19), (26), (27), (29), and (30) enables one to express the stress intensity factor for a surface flaw as a function of applied stress, crack length, crack depth, plate thickness, yield strength, and Poisson's ratio.

Figure 4 shows the factor M calculated from equations (19), (26), (27), and (30) plotted as a function of a/t and σ/Y for ν equal to 0.3, 0.4, and 0.5, and for $a/2c$ equal to 0.0, 0.25, and 0.50. The enlarging effect of the stress-free surface on the stress intensity factor for deep flaws is clearly indicated in this figure. The increase in the magnification factor with increase in the ratio of gross area stress to yield strength is due to growth of the crack-tip plastic enclave as accounted for by the plastic-zone correction term in the analysis.

With R computed according to equation (28), the condition $R \geqq t - a$ is assumed to represent a condition for which the analysis is invalid. The upper regions of the curves of figure 4 were computed for increments at a/t of 0.005, and the end points of the curves are the highest achieved values of a/t with $R < t - a$. These points are thus approximations to the condition of $R = t - a$, which is the condition for which the plastic zone is computed to have reached the opposite face of the plate.

Because of the approximations involved in the derivation of the stress intensity factor for surface-cracked plates, it is desirable to test its applicability by comparing fracture toughness values computed from fracture data having large ranges of the ratios $a/2c$, a/t, and σ/Y.

FRACTURE TOUGHNESS VALUES COMPUTED FOR SURFACE-CRACK DATA

The major usefulness of an analysis for the stress intensity factor is that it can often be used as a fracture criterion. Values of K_{Ic} computed from tests of suitable specimens have been found to agree with values of K_{Ic} computed for failed structures. If such a correlation is to exist, then values of K_{Ic} computed for a set of specimens of a given material in a given environment should be constant (independently of variations in the crack or specimen geometry). The usefulness of the analyses of references 1 and 3 and of the present report will therefore be compared by applying these analyses to specimen fracture data from the literature. The computed toughness values will be designated as $K_{Ic,\,Ir}$, $K_{Ic,\,Kob}$, and $K_{Ic,\,And}$, respectively. The relative ranges of crack geometry over which these toughness values are essentially constant will then be compared. The response of the computed values of fracture toughness to the variables of the crack geometry will be observed by fitting the constants of the following model (eq. (31)) to the results of specimen tests for particular materials and environments:

$$u = b_0 + b_2\left(\frac{a}{t}\right) + b_3\left(\frac{a}{2c}\right) + b_{22}\left(\frac{a}{t}\right)^2 + b_{33}\left(\frac{a}{2c}\right)^2 + b_{23}\left(\frac{a}{t}\right)\left(\frac{a}{2c}\right) \tag{31}$$

where u is a computed value of fracture toughness.

The response given by equation (31) can be exhibited by plotting contour lines of constant u on the coordinates of the crack geometry, namely, a/t and a/2c. Such plots are shown for values of u equal to $K_{Ic,\,Ir}$, $K_{Ic,\,Kob}$, and $K_{Ic,\,And}$. These plots distinguish the regions of the a/2c, a/t plane for which the particular K_{Ic} is relatively constant from those regions over which the computed K_{Ic} varies significantly. Comparison of such plots permits comparisons of the relative sizes of the a/2c, a/t regions for which the different analyses for K_{Ic} produce essentially constant values.

Epoxy Data

Fracture specimens of a brittle material are useful for investigating the effects of crack geometry because the complicating effects of crack-tip plasticity are minimized. Results from a large number of specimens containing semielliptical surface cracks were presented in reference 8. These specimens were prepared from a fairly brittle epoxy resin system cast into sheets 0.14 to 0.25 inch (3.6 to 6.3 mm) thick. Some properties of this material are given in table I. A reference value of K_{Ic} had been determined from single-edge-notch tension specimens (for which the stress intensity analysis is

TABLE I. - MATERIAL PROPERTIES

Material	Test environment	Poisson's ratio	Yield strength		Ultimate strength	
			ksi	kN/m^2	ksi	kN/m^2
Cast epoxy[a]	Ambient air	0.38	5.5	38	8.7	60
Aluminum alloy 2219-T87[b]	Liquid nitrogen	0.31	67.1	464	85.5	590
	Liquid hydrogen	0.36	71.5	484	92.9	641
Titanium alloy Ti-5Al-2.5Sn-ELI[c]	Liquid nitrogen	[d]0.36	177.9	813	185.5	1280
	Liquid hydrogen	[d]0.42	201.7	1390	205.7	1420

[a]CIBA Araldite 502/956; 0.14 to 0.25 in. (3.6 to 6.3 mm) thick; data from ref. 8.

[b]Longitudinal grain, 0.625 in. (16 mm) thick; data from ref. 10.

[c]Transverse grain, 0.22 in. (5.6 mm) thick; data from ref. 10.

[d]Value determined using longitudinal-grain specimens.

fairly certain), and was reported as 541.6 psi$\sqrt{\text{in.}}$ (0.596 MNm$^{-3/2}$). Based on this value the specimen dimensions far exceed the currently recommended minimum values (crack depth and specimen thickness greater than 2.5 K_{Ic}^2/Y^2, ref. 9). Surface-crack specimens had been prepared by forcing a sharp-edged tool into the surface while the specimen was stressed in bending. Minimum values of specimen length-to-width and width-to-crack-length ratios were 2 and 4, respectively. The values of a/2c and a/t achieved are shown by the plotted points of figure 5. (The contour lines of fig. 5 will be discussed in a subsequent section.)

Examination of the joint response of computed K_{Ic} to values of a/2c and a/t is readily accomplished if curves of K_{Ic} as a function of a/t can be plotted for a succession of constant values of a/2c. An approximation to this objective was achieved by partitioning the data into sets having nearly constant values of a/2c. The sets are defined by values of a/2c as follows: 0.15±0.01, 0.19±0.01, 0.23±0.01, 0.27±0.01, 0.31±0.01, and 0.35±0.01. More than half of the available data (58 of 100 tests) lie within these very narrow bands.

Computed values of $K_{Ic, Ir}$, $K_{Ic, Kob}$, and $K_{Ic, And}$ were plotted as ordinates against values of a/t as abscissa, for the previously defined approximately constant values of a/2c, for the epoxy data. These plots are shown as figures 6(a) to (f). The plots show a small downward trend of $K_{Ic, And}$, a slightly steeper downward trend for $K_{Ic, Kob}$, and a much steeper downward trend of $K_{Ic, Ir}$ with a/t at the larger values of a/t. The plots are not in conflict with the commonly made observation that a downward trend of $K_{Ic, Ir}$ occurs if a/t is larger than 0.5.

By doubling the width of the narrow a/2c bands used earlier (to ±0.02 about the same central values), all but four tests out of 100 may be included. Values of $K_{Ic, And}$ for these 96 specimens are plotted in figure 7, where the effect of both geometric variables (a/2c and a/t) may be readily seen. As mentioned earlier, there is a small downward trend of $K_{Ic, And}$ with increasing a/t. There also appears to be a slight layering tendency; that is, $K_{Ic, And}$ appears to be slightly lower for the lower values of a/2c. In addition, the random scatter appears to be fairly high, but this may be typical of cast polymeric materials. However, the reference value K_{Ic} = 541.6 psi$\sqrt{\text{in.}}$ seems to be central to the data spread of figure 7.

The response of the computed values of fracture toughness to the geometrical variables of the epoxy specimens was observed by fitting the constants of equation (31) to the results of the tests of 100 specimens. The fitted model (eq. (31)) was divided on both sides by the quantity K_{Ic} = 541.6 psi$\sqrt{\text{in.}}$ (0.596 MNm$^{-3/2}$), and contour lines for the resulting ratio were determined for values of the ratio; that is, computed fracture toughness divided by K_{Ic} of 0.8, 0.9, 1.0, 1.1, and 1.2. The plots are shown by figure 5. The closeness of the contour lines of figure 5(a) shows that values computed from the Irwin analysis for fracture toughness vary rather rapidly with a/t and a/2c;

whereas, as shown by figures 5(b) and (c), the variation of $K_{Ic, Kob}$ and $K_{Ic, And}$ is relatively less rapid with a/t and a/2c.

Data for Aluminum and Titanium Alloys

The metallic specimens of reference 10 were tested in two cryogenic liquids, and some properties of these materials in these environments are also given in table I. The values of a/t and a/2c for the metallic specimens are displayed in figures 8 to 11.

The plots of figures 8 to 11 show relatively uniform distributions of a/t over the range from 0.4 to 0.8; whereas, the values of a/2c were concentrated in two or three relatively narrow zones about discrete values of a/2c. These concentrations permitted computed values of $K_{Ic, Ir}$, $K_{Ic, Kob}$, and $K_{Ic, And}$ to be plotted for varying a/t at essentially constant values of a/2c. The results are shown in figures 12 to 19. In many cases, the values of σ/Y and a/t were larger than the largest values commonly regarded as acceptable for the Irwin analysis. The values of $K_{Ic, Kob}$ and $K_{Ic, And}$ were computed only for those specimens where computations suggested that the plastic zone had not reached the rear surface.

Some of the plots of figures 12 to 19 (particularly those for the titanium base alloy) show a downtrend of $K_{Ic, And}$ with a/t at approximately constant a/2c. In these cases, the downward trend was slightly steeper for $K_{Ic, Kob}$ and still steeper for $K_{Ic, Ir}$. For all three analyses, the responses of the computed values of K to a/t in figures 12 to 19 suggest that the computed K values vary more rapidly with a/t at the smaller values of a/2c.

Values of $K_{Ic, And}$ have been plotted against a/t in figures 13, 15, 17, and 19 for the stated materials and environments and for the values of a/2c given by the symbols. Figure 13 shows no trend of $K_{Ic, And}$ with crack geometry. Figure 15 suggests that $K_{Ic, And}$ increases slightly with a/2c, particularly at the larger values of a/t, and that $K_{Ic, And}$ decreases slightly with a/t for the smaller values of a/2c. Figure 17 also suggests that $K_{Ic, And}$ increases with a/2c at the larger values of a/t. Compared to the results for the aluminum base alloy, figures 17 and 19 for the titanium base alloy show strong decreases of $K_{Ic, And}$ with a/t for any value of a/2c.

The inconstancy of the plotted values of figure 17 suggests that the specimen dimensions might not have been adequate for a valid measurement of fracture toughness. In particular, the criterion $a > 2.5\,(K_{Ic}/Y)^2$ was advanced in reference 9 as a sufficient criterion for adequate specimen crack depth. The data of figure 17 will be examined to see how they compare with this criterion. The lowest plotted value is 46 ksi$\sqrt{\text{in.}}$ (50.5 $MNm^{-3/2}$) and thus the conceivably lowest allowable value for a/t is

$$\frac{a}{t} = \frac{2.5}{0.22}\left(\frac{46}{177.9}\right)^2 = 0.76$$

Therefore, almost all the points of figure 17 lie below this possibly too high lower limit for a/t. The conclusion must be that none of the specimens of figure 17 clearly met the criterion of reference 9.

The lowest value of $K_{Ic,\,And}$ plotted in figure 19 leads to the condition

$$\frac{a}{t} = \frac{2.5}{0.22}\left(\frac{39.5}{201.7}\right)^2 = 0.44$$

Thus some of the specimens of figure 19 might have had sufficiently large values of crack depth to furnish correct values of K_{Ic}. Inspection of figure 19 shows a cluster of approximately constant values of $K_{Ic,\,And}$ in the range of $0.60 < a/t < 0.85$ with a median value of $K_{Ic} = 43.1$ ksi $\sqrt{\text{in.}}$ (47 $\text{MNm}^{-3/2}$). For such a value of K_{Ic}, the limit on a/t is

$$\frac{a}{t} = \frac{2.5}{0.22}\left(\frac{43.1}{201.7}\right)^2 = 0.52$$

Thus, the criterion advanced in reference 9 appears to account for the continuously varying $K_{Ic,\,And}$ of figure 17 and for the division point between varying $K_{Ic,\,And}$ and constant $K_{Ic,\,And}$ in figure 19.

Similar trends were reported in the literature for titanium alloys and maraging steels for $K_{Ic,\,Ir}$, even with $a/t < 0.5$. Some data for maraging steels and discussion of the trends are given on pages 30 to 33 of reference 9.

The model, equation (31), was fitted to the computed values of K for the aluminum and titanium alloy specimens and contour lines of fitted K were plotted as shown by figures 8 to 11. (In the case of $K_{Ic,\,And}$ for the aluminum base alloy tested in liquid nitrogen, none of the coefficients of variables in eq. (31) were statistically significant and no contour lines were plotted.)

The plotted points of figures 8 to 11 show the ranges of conditions of the experiments and therefore show the ranges over which the model should be assumed to be valid. Contour lines close together show sensitivity of the computed K to the geometry. In most cases, the contour lines for $K_{Ic,\,Ir}$ are closer together than were the comparable lines for $K_{Ic,\,Kob}$, and the $K_{Ic,\,Kob}$ lines are closer than the $K_{Ic,\,And}$ lines. Therefore, $K_{Ic,\,And}$ is concluded to be less sensitive to specimen geometry than the other analyses.

In some cases, the contour lines were parallel or approximately parallel to the a/2c axis, showing an insensitivity of the computed K to a/2c, but a sensitivity to a/t. In some cases, the reverse effect is observed. In all cases, for any given material and environment, the orientation of the contour lines for all the analyses was about the same;

however, orientation differed markedly for the two materials, the computed fracture toughness being somewhat sensitive to $a/2c$ for the aluminum (fig. 9) and being clearly sensitive to a/t for the titanium (figs. 10 and 11).

Ranges of Approximately Constant Fracture Toughness

In figure 5(c) the contour lines labeled 0.9 and 1.1 bound a region (between them) where the value of $K_{Ic,\,And}$ is within ±10 percent of the edge-crack value. For simplicity, this region can be closely approximated by the rectangular region bounded by $0.15 \leq (a/2c) \leq 0.35$, $0.45 \leq (a/t) \leq 0.85$. Within these limits, then, values of $K_{Ic,\,And}$ were approximately constant and approximately equal to the K_{Ic} value obtained from edge-crack specimens. No reference K_{Ic} values were reported for the 2219-T87 aluminum alloy. However, the tests in liquid nitrogen (not plotted; see preceeding section) and the contour plot of figure 9(c) suggest that the range of constant $K_{Ic,\,And}$ (±10 percent) is at least as large as that established for the epoxy specimens. This may also be seen in figures 13 and 15, where the average value of $K_{Ic,\,And}$ is about 45 ksi$\sqrt{\text{in.}}$ (49 $\text{MNm}^{-3/2}$) in either cryogenic liquid.

Application of the criterion of reference 9 suggests that the following minimum values of crack depth apply:

For the conditions of figure 13,

$$a_{min} = 2.5\left(\frac{45}{67.1}\right)^2 = 1.12$$

For the conditions of figure 15,

$$a_{min} = 2.5\left(\frac{45}{71.5}\right)^2 = 0.99$$

Both these values exceed the specimen thickness; however, the approximately constant values of $K_{Ic,\,And}$ of figures 13 and 15 seem to have reasonable magnitudes.

For the titanium-5Al-2.5Sn alloy tested in liquid nitrogen and in liquid hydrogen (figs. 10 and 11), the values of $K_{Ic,\,Ir}$, $K_{Ic,\,Kob}$, and $K_{Ic,\,And}$ varied quite rapidly with a/t except for the $K_{Ic,\,And}$ for liquid hydrogen (fig. 11(c)). Again, no $K_{Ic,\,Kob}$ or $K_{Ic,\,And}$ values were computed if either analysis indicated that the plastic zone had reached the rear face. The fact that most of the resulting K_{Ic} values varied considerably with a/t suggests that a more severe restriction on specimen geometry is needed to identify specimens that will give constant K_{Ic} values in the case of titanium-5Al-2.5Sn. The criterion $a > 2.5\,(K_{Ic}/Y)^2$ as advanced in reference 9 is appropriate to the

present data for the titanium alloy but appears unnecessarily restrictive for the aluminum alloy.

CONCLUDING REMARKS

In an early investigation, G. R. Irwin (ref. 1) derived an expression for the stress intensity factor for surface cracks in a plate with crack depths less than half the plate thickness. The present and previous investigations have shown that apparent fracture toughness values computed according to the Irwin analysis decrease with increasing crack depth-to-thickness ratio as this ratio increases beyond about 0.5.

The method proposed in this investigation for computing stress intensity factors for deep part-through cracks attempts to account for the effect of crack-tip plasticity and the effect of the free surface opposite the crack. The magnification factor was expressed as a function of the ratio of applied stress to yield strength, the ratio of crack depth to crack length, the ratio of crack depth to sheet thickness, and Poisson's ratio. In addition, the method contains a criterion for deciding if plasticity has progressed from the crack tip to the defect-free surface. If this condition is met or exceeded, the analysis is regarded as invalid for the computation of elastic stress intensity factors or for plane-strain fracture toughness.

The proposed analysis was applied to some surface-crack specimen data from the literature. Computed values of the fracture toughness were reported for those specimens for which analysis indicated that fracture occurred prior to the spread of a plastic zone to the defect-free surface. The materials and environments included a cast epoxy in room-temperature air, and aluminum and titanium alloys in liquid nitrogen and liquid hydrogen. Except for the titanium base alloy, the computed critical stress intensity factor was found to remain essentially constant (constant within ±10 percent) over wide variations of the crack depth-to-length ratio (0.15 to 0.35) and over wide variations of the crack-depth-to-specimen-thickness ratio (0.45 to 0.85).

Lewis Research Center,
National Aeronautics and Space Administration,
Cleveland, Ohio, July 6, 1970,
124-08.

APPENDIX A

PLASTIC-ZONE CORRECTION FACTOR FOR COPLANAR THROUGH-CRACKS

The elastic stress function for a remotely tensioned plate having a series of equally spaced, coplanar through-cracks is given by Westergaard in reference 11.

In this solution, the component of stress directly ahead of the crack that acts in a direction normal to the crack plane is given as a function of the distance r from the crack tip in reference 12 as

$$\sigma_y = \sigma \left[1 - \frac{\sin^2 \frac{\pi b}{W}}{\sin^2 \frac{\pi(b + r)}{W}} \right]^{-1/2} \tag{A1}$$

in which b is the half-length of the crack, W is the spacing of crack centers, and σ is the remote tensile stress. If the elastic solution for stress near the crack tip given by equation (A1) is applied to ductile materials, then under sufficient load, some region of material at the crack would be computed to be above the yield point. The appropriate assumption is that yielding takes place along some distance R from the crack tip as shown in figure 20. Equilibrium conditions require that stress in excess of the yield stress must be borne by adjacent elastic material. The resulting stress distribution for a nonhardening material might be similar to that indicated by the dashed curve in figure 20. Clearly, in this case, equation (A1) does not describe the stress distribution within the yielded region, nor does it accurately apply to the surrounding elastic region. In reference 6, Irwin suggests that the effect of stress relaxation is equivalent to that of an increase in crack length. This effect is shown in figure 20 in which the half-length of the equivalent crack is represented by $\bar{b}$ which is longer than the half-length of the actual crack by an amount λR, where λR is a fraction of R. The stress distribution of equation (A1) should now be referred to a new coordinate system in which $\bar{r}$ is the distance from the end of the equivalent crack, in which case

$$\sigma_y = \sigma \left[1 - \frac{\sin^2 \frac{\pi \bar{b}}{W}}{\sin^2 \frac{\pi(\bar{b} + \bar{r})}{W}} \right]^{-1/2} \tag{A2}$$

From figure 20,

$$\bar{b} = b + \lambda R \tag{A3}$$

and

$$\bar{R} = (1 - \lambda)R \tag{A4}$$

At the elastic-plastic interface, $\bar{r}$ equals $\bar{R}$ and σ_y equals σ_Y. From equations (A2) to (A4),

$$\sigma_Y = \sigma \left[1 - \frac{\sin^2 \frac{\pi b}{W} \left(1 + \frac{\lambda R}{b} \right)}{\sin^2 \frac{\pi b}{W} \left(1 + \frac{R}{b} \right)} \right]^{-1/2} \tag{A5}$$

Then the plastic-zone correction factor can be derived from equation (A5) as

$$1 + \lambda \frac{R}{b} = \frac{W}{\pi b} \arcsin \left\{ \left[1 - \left(\frac{\sigma}{\sigma_Y} \right)^2 \right]^{1/2} \left[\sin \frac{\pi b \left(1 + \frac{R}{b} \right)}{W} \right] \right\} \tag{A6}$$

APPENDIX B

LENGTH OF PLASTIC ENCLAVE FOR COPLANAR THROUGH-CRACKS

D. S. Dugdale (ref. 13) has derived an expression for the length of the plastic enclave at the tip of a crack in an infinitely wide plate. The following derivation is an extension of his analysis to a plate having a series of coplanar cracks.

Consider a series of coplanar cracks of length 2b spaced W from center to center in a plate subjected to a remote tensile stress σ. For a ductile material, consider that yielding occurs at the crack tip and extends a distance R in front of the crack, as shown in figure 21. As in the Dugdale analysis, the plastic zone is assumed to be an extension of the crack.

If the entire plastic zone is considered as part of the crack, the total length of the resulting virtual crack is $2l = 2(b + R)$. The stress ahead of the virtual crack (fig. 22) is approximated by equation (B1), which can be derived from the Westergaard stress function for a series of coplanar cracks and is given in reference 12 as

$$\sigma_{1y} = \sigma \left[1 - \frac{\sin^2 \frac{\pi l}{W}}{\sin^2 \frac{\pi(l + r)}{W}} \right]^{-1/2} \tag{B1}$$

Close to the virtual crack tip ($r/l \ll 1$) the stress component is

$$\sigma_{1y} = \sigma \left(\frac{W}{2\pi r} \tan \frac{\pi l}{W} \right)^{1/2} \tag{B2}$$

The stress ahead of the virtual crack is less than that given by equation (B2) because the material within the plastic enclave partially constrains displacement of the virtual crack border. This constraining effect can be idealized as indicated in figure 23 in which a stress σ_p in the plastic enclave acts on the virtual crack border and tends to close the crack. An expression for the stress ahead of the virtual crack due to the action of σ_p is derived by first considering the stress in front of a crack of length l caused by a pair of negative splitting forces P acting on the crack border as shown in figure 24. The stress distribution on the right end of the crack caused by the splitting forces can be derived from the stress function in reference 14 as

$$\sigma_{2y}^{R}(P) = \frac{-P \cos \frac{\pi\xi}{W} \sqrt{\sin^2 \frac{\pi l}{W} - \sin^2 \frac{\pi\xi}{W}}}{W \sin \frac{\pi(l + r)}{W} \left[\sin \frac{\pi(l + r)}{W} - \sin \frac{\pi\xi}{W}\right] \sqrt{1 - \frac{\sin^2 \frac{\pi l}{W}}{\sin^2 \frac{\pi(l + r)}{W}}}} \tag{B3}$$

Similarly, the additional stress on the right side of the crack caused by a pair of splitting forces P' on the left side of the crack is

$$\sigma_{2y}^{L}(P') = \frac{-P' \cos \frac{\pi\xi}{W} \sqrt{\sin^2 \frac{\pi l}{W} - \sin^2 \frac{\pi\xi}{W}}}{W \sin \frac{\pi(l + r)}{W} \left[\sin \frac{\pi(l + r)}{W} + \sin \frac{\pi\xi}{W}\right] \sqrt{1 - \frac{\sin^2 \frac{\pi l}{W}}{\sin^2 \frac{\pi(l + r)}{W}}}} \tag{B4}$$

For values of r very near the crack tip ($r \ll l$), equations (B3) and (B4) reduce to

$$\sigma_{2y}^{R}(P) = \frac{-\frac{P}{W} \cos \frac{\pi\xi}{W}}{\left(\frac{2\pi r}{W} \sin \frac{\pi l}{W} \cos \frac{\pi l}{W}\right)^{1/2}} \left(\frac{\sin \frac{\pi l}{W} + \sin \frac{\pi\xi}{W}}{\sin \frac{\pi l}{W} - \sin \frac{\pi\xi}{W}}\right)^{1/2} \tag{B5}$$

and

$$\sigma_{2y}^{L}(P') = \frac{-\frac{P'}{W} \cos \frac{\pi\xi}{W}}{\left(\frac{2\pi r}{W} \sin \frac{\pi l}{W} \cos \frac{\pi l}{W}\right)^{1/2}} \left(\frac{\sin \frac{\pi l}{W} - \sin \frac{\pi\xi}{W}}{\sin \frac{\pi l}{W} + \sin \frac{\pi\xi}{W}}\right)^{1/2} \tag{B6}$$

The stress ahead of the crack due to σ_P can be derived by treating the splitting forces P and P' as Green's functions. When equations (B5) and (B6) are added and integrated between $\xi = b$ and $\xi = l$ to account for splitting forces distributed at both ends of the crack, the resulting stress ahead of the crack, as shown in figure 25, is

$$\sigma_{2y} = \sigma_{2y}^{L} + \sigma_{2y}^{R} = \frac{\frac{-2}{W}\left(\sin\frac{\pi l}{W}\right)\frac{W}{\pi}}{\left(\frac{2\pi r}{W}\sin\frac{\pi l}{W}\cos\frac{\pi l}{W}\right)^{1/2}} \int_{b}^{l} \frac{\sigma_P \cos\frac{\pi\xi}{W}\, d\left(\frac{\pi\xi}{W}\right)}{\left(\sin^2\frac{\pi l}{W} - \sin^2\frac{\pi\xi}{W}\right)^{1/2}} \tag{B7}$$

Taking σ_P as constant and equal to the yield stress σ_Y and completing the integration gives

$$\sigma_{2y} = \frac{-2\sigma_Y}{\pi}\sqrt{\frac{W}{2\pi r}\tan\frac{\pi l}{W}}\left(\frac{\pi}{2} - \arcsin\frac{\sin\frac{\pi b}{W}}{\sin\frac{\pi l}{W}}\right) \tag{B8}$$

The total stress near the tip of the crack is obtained by adding equations (B2) and (B8)

$$\sigma_y = \sigma_{1y} + \sigma_{2y} = \sqrt{\frac{W}{2\pi r}\tan\frac{\pi l}{W}}\left(\sigma - \sigma_Y + \frac{2\sigma_Y}{\pi}\arcsin\frac{\sin\frac{\pi b}{W}}{\sin\frac{\pi l}{W}}\right) \tag{B9}$$

At the elastic-plastic boundary (r = 0), the stress σ_y is finite. Hence, the bracketed term on the right side of equation (B9) must equal zero; that is,

$$\sigma - \sigma_Y + \frac{2\sigma_Y}{\pi}\arcsin\left(\frac{\sin\frac{\pi b}{W}}{\sin\frac{\pi l}{W}}\right) = 0 \tag{B10}$$

Since $l = b + R$, equation (B10) can be rearranged to give the plastic-zone length as a function of b, W, σ_Y, and σ

$$\frac{R}{b} = \frac{W}{\pi b}\arcsin\left(\sin\frac{\pi b}{W}\sec\frac{\pi}{2}\frac{\sigma}{\sigma_Y}\right) - 1 \tag{B11}$$

It should be noted that an equation of similar form can be derived from the results of the dislocation stress analysis of reference 15, which treats an infinite array of coplanar cracks in a plate subjected to remote shear stress.

APPENDIX C

CONSTRAINT OF PLASTIC ENCLAVE

An approximation to the effect of a stress-free surface on the stress ratio σ_X/σ_Y at the elastic-plastic interface can be made by use of the exact solution for a plate cut by a series of coplanar through-cracks as described in appendixes A and B. For this geometry, the stresses σ_x and σ_y directly ahead of the crack are given in reference 12 as

$$\sigma_y = \sigma \left(1 - \frac{\sin^2 \frac{\pi b}{W}}{\sin^2 \frac{\pi x}{W}} \right)^{-1/2} \tag{C1}$$

and

$$\sigma_x = \sigma \left(1 - \frac{\sin^2 \frac{\pi b}{W}}{\sin^2 \frac{\pi x}{W}} \right)^{-1/2} - \sigma_{0x} \tag{C2}$$

in which σ_{0x} is a uniform stress in the x-direction. Then the ratio of the stress components is

$$\frac{\sigma_x}{\sigma_y} = 1 - \frac{\sigma_{0x}}{\sigma} \left(1 - \frac{\sin^2 \frac{\pi b}{W}}{\sin^2 \frac{\pi x}{W}} \right)^{1/2} \tag{C3}$$

The condition of a stress-free surface requires that σ_x equal zero at x equal to W/2. By substituting $\sigma_x = 0$ and $x = W/2$ in equation (C2), σ_{0x} is found to be equal to $\sigma \left[1 - \sin^2(\pi b/W) \right]^{-1/2}$. When this value is substituted for σ_{0x} in equation (C3), the boundary condition for the stress-free surface is met at the point (W/2, 0) directly ahead of the crack and is approximated in the region near that point. By making this substitution and solving equations (C1) and (C3),

$$\frac{\sigma_x}{\sigma_y} = 1 - \frac{\dfrac{\sigma}{\sigma_y}}{\left(1 - \sin^2 \dfrac{\pi b}{W}\right)^{1/2}} \tag{C4}$$

At the elastic-plastic interface $\sigma_x = \sigma_X$ and $\sigma_y = \sigma_Y$ so that

$$\frac{\sigma_X}{\sigma_Y} = 1 - \frac{\dfrac{\sigma}{\sigma_Y}}{\left(1 - \sin^2 \dfrac{\pi b}{W}\right)^{1/2}} \tag{C5}$$

When crack-tip plasticity is taken into account, the dimension b should be replaced by $b(1 + \lambda R/b)$ as given by equation (A6) of appendix A. Thus

$$\frac{\sigma_X}{\sigma_Y} = 1 - \frac{\sigma}{\sigma_Y}\left\{1 - \left[1 - \left(\frac{\sigma}{\sigma_Y}\right)^2\right] \sin^2 \frac{\pi b\left(1 + \dfrac{R}{b}\right)}{W}\right\}^{-1/2} \tag{C6}$$

The plastic enclave length R is given by equation (B11) of appendix B, which when solved with equation (C6) results in

$$\frac{\sigma_X}{\sigma_Y} = 1 - \frac{\sigma}{\sigma_Y}\left\{1 - \left[1 - \left(\frac{\sigma}{\sigma_Y}\right)^2\right]\left(\sin \frac{\pi b}{W}\right)^2 \left(\sec \frac{\pi \sigma}{2\sigma_Y}\right)^2\right\}^{-1/2} \tag{C7}$$

APPENDIX D

COMPUTATIONAL PROCEDURES FOR PROPOSED MAGNIFICATION FACTOR

The equations involved in the computation of M are (19), (26), (27), and (30). The quantity Y/σ_Y of equation (27) cannot be obtained as an explicit function of the variables remaining after the elimination of σ_X/σ_Y from equations (19) and (26). The lack of an explicit function for σ/σ_Y requires the use of an iterative procedure. The procedure used was as follows:

Let

$$q_1 = \cos\left(\frac{\pi}{2}\frac{\sigma}{\sigma_Y}\right) = \cos\left(\frac{\pi}{2}\frac{\sigma}{Y}\frac{Y}{\sigma_Y}\right) \tag{D1}$$

$$q_2 = \sin\left(\frac{\pi}{2}\frac{a^*}{t}\right) \tag{D2}$$

$$q_3 = 1 - \left(\frac{\sigma}{\sigma_Y}\right)^2 = 1 - \left(\frac{\sigma}{Y}\frac{Y}{\sigma_Y}\right)^2 \tag{D3}$$

$$q = q_3\left(\frac{q_2}{q_1}\right)^2 \tag{D4}$$

where, in general,

$$\frac{\sigma}{\sigma_Y} = \frac{\sigma}{Y}\frac{Y}{\sigma_Y} \tag{D5}$$

and from equation (25)

$$\frac{a^*}{t} = \frac{1}{\Phi^2}\frac{a}{t} \tag{D6}$$

As an initial approximation let

$$\frac{Y}{\sigma_Y} = \left[3 - \frac{9}{4(1 - \nu + \nu^2)}\right]^{1/2} \tag{D7}$$

With the preceding value of Y/σ_Y, equation (26) can be solved for σ_X/σ_Y as follows:

$$\frac{\sigma_X}{\sigma_Y} = 1 - \frac{\frac{\sigma}{Y}\frac{Y}{\sigma_Y}}{(1 - q)^{1/2}} \tag{D8}$$

and with the preceding value of σ_X/σ_Y, and improved value of Y/σ_Y can be obtained from equation (19) as follows:

$$\frac{Y}{\sigma_Y} = \left[(1 - \nu + \nu^2)\left(1 + \frac{\sigma_X}{\sigma_Y}\right)^2 - 3\frac{\sigma_X}{\sigma_Y}\right]^{1/2} \tag{D9}$$

This improved value of Y/σ_Y is substituted in the preceding equations for q_1 and q_3 and an improved value of σ_X/σ_Y is computed leading to a still further improved value of Y/σ_Y. This type of iteration was continued i times until

$$\left|\left(\frac{Y}{\sigma_Y}\right)_i - \left(\frac{Y}{\sigma_Y}\right)_{i-1}\right| < 0.001 \tag{D10}$$

However, if the preceding specification was not met before $i = 50$, the operation was judged uncomputable.

On suitable convergence of the computation of Y/σ_Y, a value of

$$Q = \left(1 + \lambda\frac{R}{a^*}\right)\frac{\pi}{2}\frac{a^*}{t}$$

was computed from equation (27); namely,

$$Q = \arcsin\left(q_3^{1/2}\frac{q_2}{q_1}\right) \tag{D11}$$

and from equation (30)

$$M = \left[1 + 0.12\left(1 - \frac{a}{c}\right)\right]\left(\frac{\tan Q}{\frac{\pi}{2}\frac{a^*}{t}}\right)^{1/2} \tag{D12}$$

Let $K_0 = \sigma(\pi a^*)^{1/2}$. Then from equation (29)

$$K_{I,\,And} = K_0 M \tag{D13}$$

From equation (28), the fraction of the uncracked region penetrated by the plastic zone is

$$\frac{R}{t-a} = \frac{2}{\pi}\frac{t}{t-a}\arcsin\left(\frac{q_2}{q_1}\right) - \frac{a^*}{t-a} \tag{D14}$$

APPENDIX E

COMPUTATIONAL PROCEDURES USING KOBAYASHI-MOSS ANALYSIS

An expression for the stress intensity factor was given as equation (4) in reference 3 as follows:

$$K_{I,\,Kob} = M_e M_p \sqrt{\pi}\, \sigma \frac{\sqrt{a}}{\Phi} \tag{E1}$$

The value of M_e is called the elastic magnification factor and is given by

$$M_e = M_1 M_h \tag{E2}$$

where M_h is defined to be a magnification factor due to the stress-free back surface and where M_1 is defined to be the magnification factor due to the stress-free front surface

$$M_1 = 1.0 + 0.12\left(1.0 - \frac{a}{2c}\right)^2 \tag{E3}$$

In order to provide for the computer reduction of data from experiments, a polynomial approximation was developed for M_h from curves in an unpublished Boeing Company report. The approximation is as follows:

If $0.3 \leqq \frac{a}{t} < 0.77$,

$$M_h = 0.951 + 0.327\left(\frac{a}{t}\right) + 0.080\left(\frac{a}{2c}\right) - 0.832\left(\frac{a}{t}\right)^2 + 0.362\left(\frac{a}{t}\right)\left(\frac{a}{2c}\right) - 0.580\left(\frac{a}{2c}\right)^2$$

$$+ 1.010\left(\frac{a}{t}\right)^3 - 1.136\left(\frac{a}{t}\right)^2\left(\frac{a}{2c}\right) + 0.701\left(\frac{a}{t}\right)\left(\frac{a}{2c}\right)^2 + 0.357\left(\frac{a}{2c}\right)^3 \tag{E4}$$

If $0.77 \leqq \frac{a}{t} \leqq \left[0.77 + 0.3\left(\frac{a}{2c}\right)\right]$,

$$M_h = 0.920 + 0.591\left(\frac{a}{t}\right) + 0.04\left(\frac{a}{2c}\right) - 1.581\left(\frac{a}{t}\right)^2 + 0.937\left(\frac{a}{t}\right)\left(\frac{a}{2c}\right) - 0.923\left(\frac{a}{2c}\right)^2 + 1.635\left(\frac{a}{t}\right)^3 - 1.841\left(\frac{a}{t}\right)^2\left(\frac{a}{2c}\right) + 0.958\left(\frac{a}{t}\right)\left(\frac{a}{2c}\right)^2 + 0.600\left(\frac{a}{2c}\right)^3 \quad \text{(E5)}$$

If $\left[0.77 + 0.3\left(\frac{a}{2c}\right)\right] < \frac{a}{t} \leqq 0.97$,

$$M_h = 2.441 - 3.455\left(\frac{a}{t}\right) + 4.144\left(\frac{a}{2c}\right) - 5.093\left(\frac{a}{t}\right)\left(\frac{a}{2c}\right) - 2.029\left(\frac{a}{2c}\right)^2 + 2.919\left(\frac{a}{t}\right)^3 + 3.046\left(\frac{a}{2c}\right)^3 \quad \text{(E6)}$$

No approximations were developed for the ranges $0.0 \leqq a/t < 0.3$ or $0.97 < a/t \leqq 1.0$ since no experimental results were available for these regions.

Values of M_e were computed for several values of $a/2c$ and a/t and the results are represented by the dashed lines of figure 26. The solid lines of figure 26 represent the results given in figure 2 of reference 3.

In reference 3, b is defined as the radius of a penny-shaped crack that is equivalent to the existing elliptical crack, d is defined as an extended crack radius of a Dugdale model, and σ_0 is defined as "the maximum uniaxial tensile stress prescribed at the physical crack tip of $r = a$." Equations (6), (7b), and (7a) of reference 3 give relations among the variables as follows:

$$b = \left(\frac{\frac{\pi}{2}}{\Phi}\right)^2 a \quad \text{(E7)}$$

$$m = 1 - \frac{Y}{\sigma_0} \quad \text{(E8)}$$

$$\frac{\sigma}{\sigma_0} = \left(1 - \frac{b^2}{d^2}\right)^{1/2} + \frac{m}{2\left(1 - \frac{b}{d}\right)}\left[\frac{b}{d}\left(1 - \frac{b^2}{d^2}\right)^{1/2} - \frac{\pi}{2} + \arcsin\frac{b}{d}\right] \tag{E9}$$

The analysis as thus far presented contains one more unknown than the number of equations. This difficulty is easily remedied if either m or σ_0 can be regarded as known. In the data reduction of the present investigation, m was assumed to be unknown and σ_0 was assumed to be the ultimate tensile strength of the material.

The analysis was assumed to be invalid, and values of K_I were assumed to be not computable for the condition

$$d \geqq b + t - a \tag{E10}$$

(This condition is to be compared with eq. (9) of ref. 3.)

The value of M_p is to be computed from equation (8) of reference 3, which is

$$M_p^2 = \frac{Y \arccos\frac{b}{d}}{\sigma(1 - m)} + \left\{\frac{d}{b} - \frac{Y}{\sigma(1 - m)}\left[\left(\frac{d}{b}\right)^2 - 1\right]^{1/2}\right\} \tag{E11}$$

APPENDIX F

SYMBOLS

a	depth of surface crack or half-depth of internal crack
a^*	a/Φ^2
b	half-length of through-crack
$\bar{b}$	half-length of equivalent crack (fig. 20)
b_0, b_i, b_{ij}	coefficients of eq. (31)
c	half-length of surface crack or internal crack
i, j	integers
E	modulus of elasticity
K_I	opening-mode stress intensity factor
K_{Ic}	plane-strain fracture toughness
$K_{Ic, And}$	fracture toughness computed according to this report
$K_{Ic, Ir}$	fracture toughness computed according to ref. 1
$K_{Ic, Kob}$	fracture toughness computed according to ref. 3
K_{I0}	stress intensity factor for surface crack, uncorrected for plasticity or plate thickness
l	half length of virtual crack
M	magnification factor for semielliptical surface crack
M_i	magnification factor for long internal elliptical crack
P, P'	negative splitting force per unit thickness
R	extent of plastic zone in plane of crack
$\bar{R}$	equivalent plastic zone, eq. (A4)
r	radial distance from actual or virtual crack tip
$\bar{r}$	distance from end of equivalent crack (fig. 20)
t	sheet thickness
W	coplanar through-crack spacing
x, y, z	Cartesian coordinates (fig. 1)
Y	uniaxial yield strength

ϵ_x, ϵ_y, ϵ_z	conventional elastic strain components in x-, y-, and z-directions, respectively (fig. 1)
λ	equivalent crack length multiplier
ν	Poisson's ratio
ξ	distance of negative splitting forces from crack centerline
σ	uniform remote gross area stress acting normal to plane of crack
σ_P	stress in plastic enclave
σ_x, σ_y, σ_z	stresses in x-, y-, and z-directions, respectively
σ_X, σ_Y, σ_Z	stresses in x-, y-, and z-directions, respectively, at elastic-plastic interface
Φ	complete elliptic integral of second kind
φ	coordinate angle (fig. 1)
τ_{XY}, τ_{XZ}, τ_{YZ}	components of shear stress at elastic-plastic interface

REFERENCES

1. Irwin, G. R.: Crack-Extension Force for a Part-Through Crack in a Plate. J. Appl. Mech., vol. 84, no. 4, Dec. 1962, pp. 651-654.

2. Tiffany, Charles F.; Masters, J. N.; and Pall, F. A.: Some Fracture Considerations in the Design and Analysis of Spacecraft Pressure Vessels. Paper C6-2.3, ASM, Oct. 1966.

3. Kobayashi, A. S.; and Moss, W. L.: Stress Intensity Magnification Factors for Surface-Flawed Tension Plate and Notched Round Tension Bar. Fracture 1969-Proceedings of the Second International Conference on Fracture, Brighton, England, Apr. 13-18, 1969, pp. 31-45, disc., p. 905.

4. Irwin, G. R.: Fracture. Encyclopedia of Physics. Vol. VI. S. Flügge, ed., Springer-Verlag, 1958, pp. 551-590

5. Paris, Paul C.; and Sih, George C.: Stress Analysis of Cracks. Fracture Toughness Testing and Its Applications. Spec. Tech. Publ. No. 381, ASTM, 1965, pp. 30-83.

6. Irwin, G. R.: Plastic Zone Near a Crack and Fracture Toughness. Proceedings of the Seventh Sagamore Ordnance Materials Research Conference, Syracuse University Research Institute, Aug. 16-19, 1960, pp. IV-63 to IV-78.

7. Anderson, R. B.: Plastic Strain at the Tip of a Crack Related to Fracture Mechanics. Ph. D. Thesis, Carnegie Institute of Technology, 1964.

8. Larson, Lanny Jay: Depth Effect for Semi-Elliptical Surface Flaws. Master's Thesis, Colorado State Univ., Aug. 1968.

9. Brown, W. F., Jr.; and Srawley, J. E.: Plane Strain Crack Toughness Testing of High Strength Metallic Materials. Spec. Tech. Publ. No. 410, ASTM, 1967.

10. Masters, J. N.; Haese, W. P.; and Finger, R. W.: Investigation of Deep Flaws in Thin Walled Tanks. Boeing Co. (NASA CR-72606), Dec. 1969.

11. Westergaard, H. M.: Bearing Pressures and Cracks. J. Appl. Mech., vol. 6, no. 2, June 1939, pp. A-49 - A-53.

12. Report of Special ASTM Committee: Fracture Testing of High-Strength Sheet Materials. ASTM Bull., no. 243, Jan. 1960, pp. 29-51.

13. Dugdale, D. S.: Yielding of Steel Sheets Containing Slits. J. Mech. Phys. Solids, vol. 8, no. 2, 1960, pp. 100-104.

14. Irwin, George R.: Analytical Aspects of Crack Stress Field Problems. T. & A. M. Rep. 213, Dept. Theoretical and Appl. Mech., University of Illinois, Mar. 1962.

15. Bilby, B. A.; Cottrell, A. H.; Smith, E.; and Swinden, K. H.: Plastic Yielding From Sharp Notches. Proc. Roy. Soc. (London), vol. 279, no. 1376, May 12, 1964, pp. 1-9.

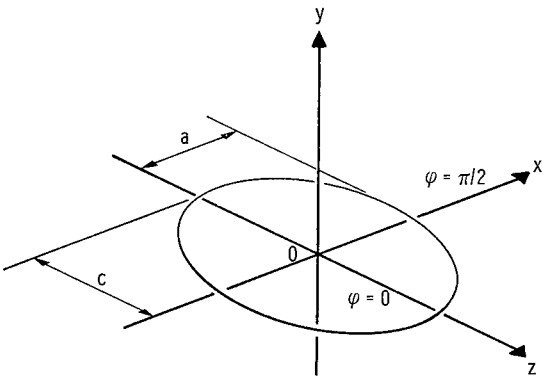

Figure 1. - Dimensions of crack and orientation of coordinate axes with respect to crack.

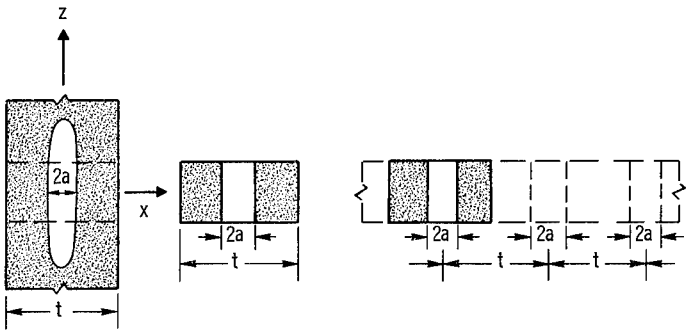

(a) Long elliptical crack. (b) Straight-front through-crack. (c) Series of coplanar straight-front through-cracks.

Figure 2. - Approximation of crack-front conditions for a long elliptical flaw in a plate of thickness t by crack-front conditions for a series of coplanar cracks.

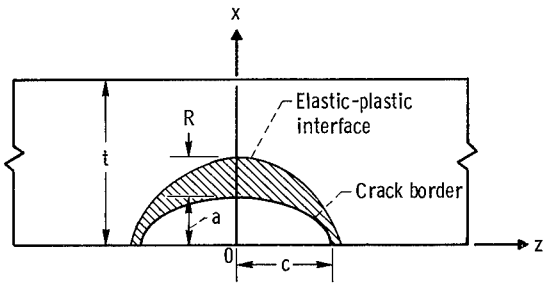

Figure 3. - Crack geometry including plastic enclave.

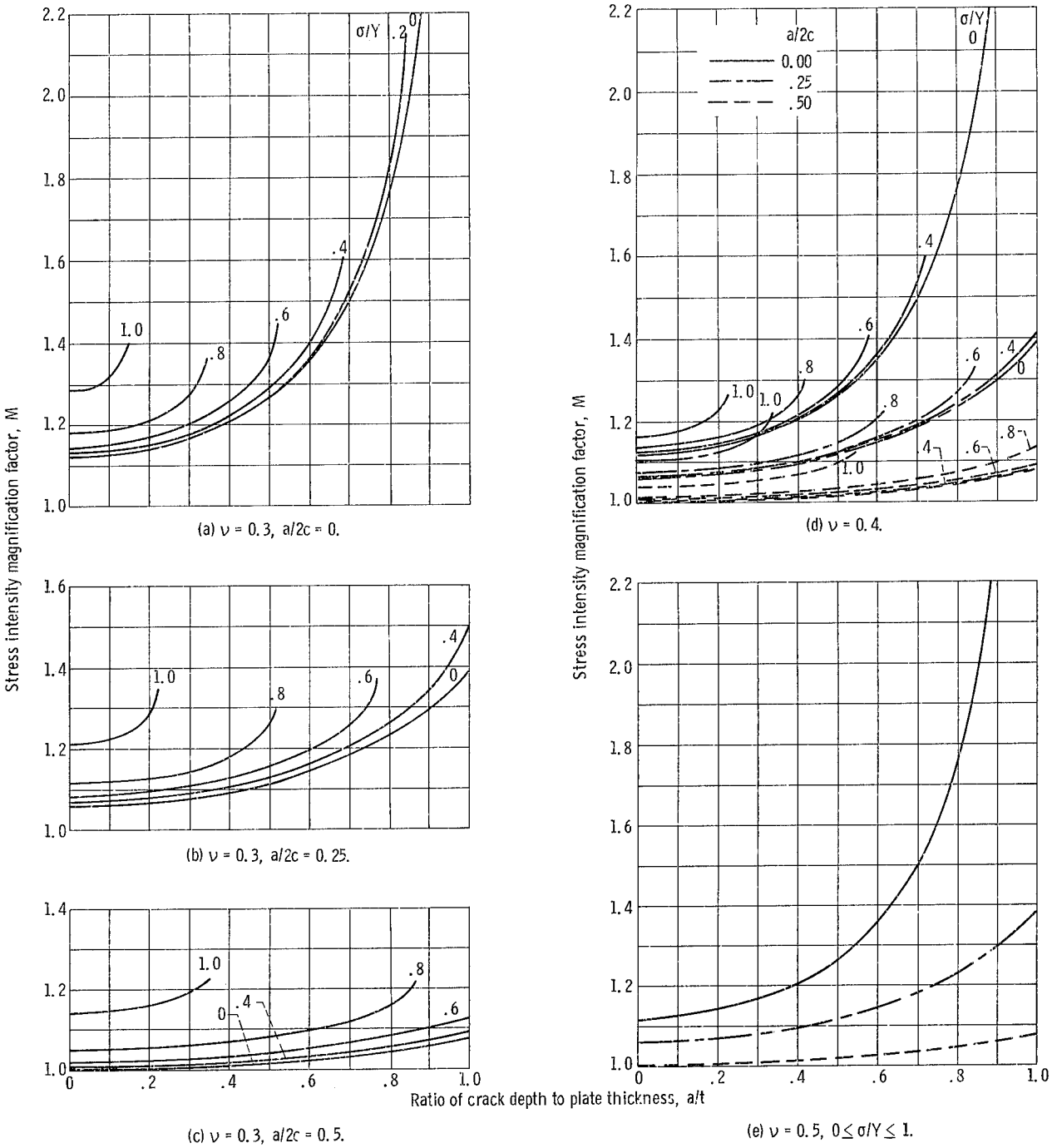

Figure 4. - Stress intensity magnification factor (eq. (30)), for various values of Poisson's ratio ν, the ratio of crack depth to crack length a/2c, and the ratio of applied stress to yield strength σ/Y.

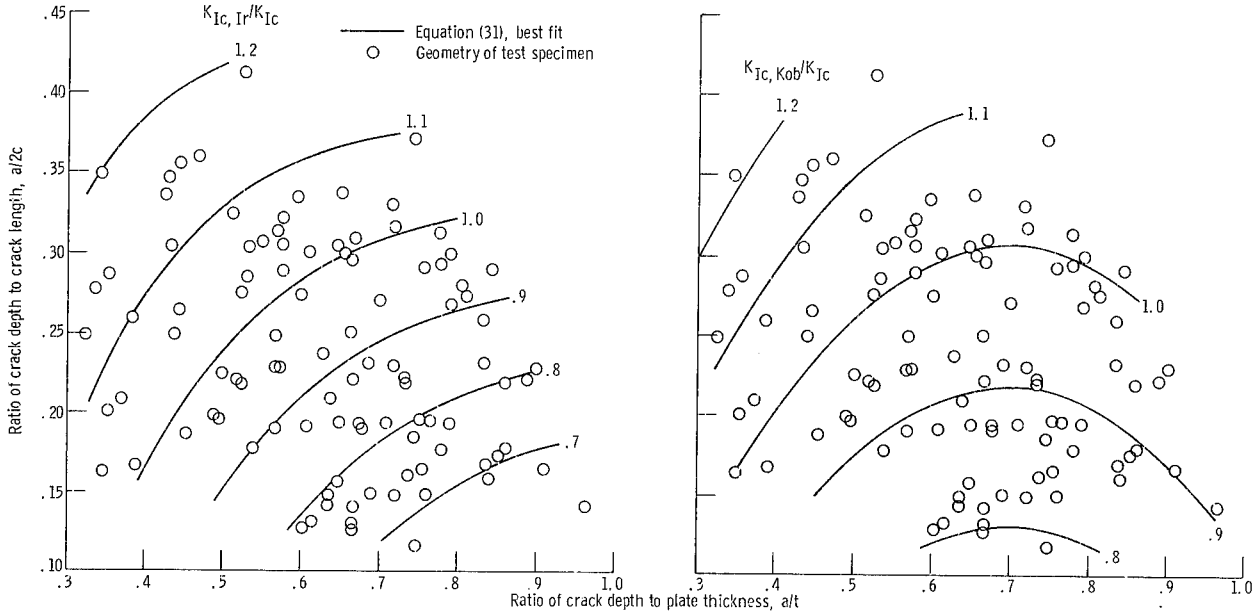

(a) Fracture toughness computed according to reference 1.

(b) Fracture toughness computed according to reference 3.

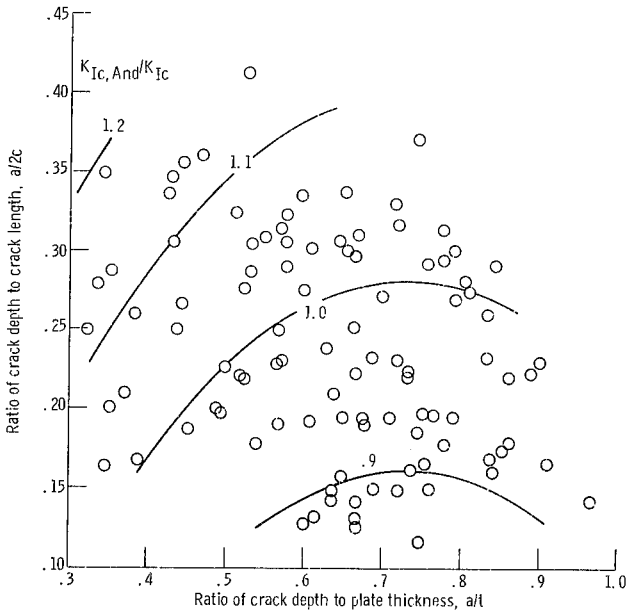

(c) Fracture toughness computed according to this report (eqs. (29) and (30)).

Figure 5. - Contour lines of constant computed fracture toughness ratio for epoxy specimens, tested in air. Crack geometry shown by plotted points.

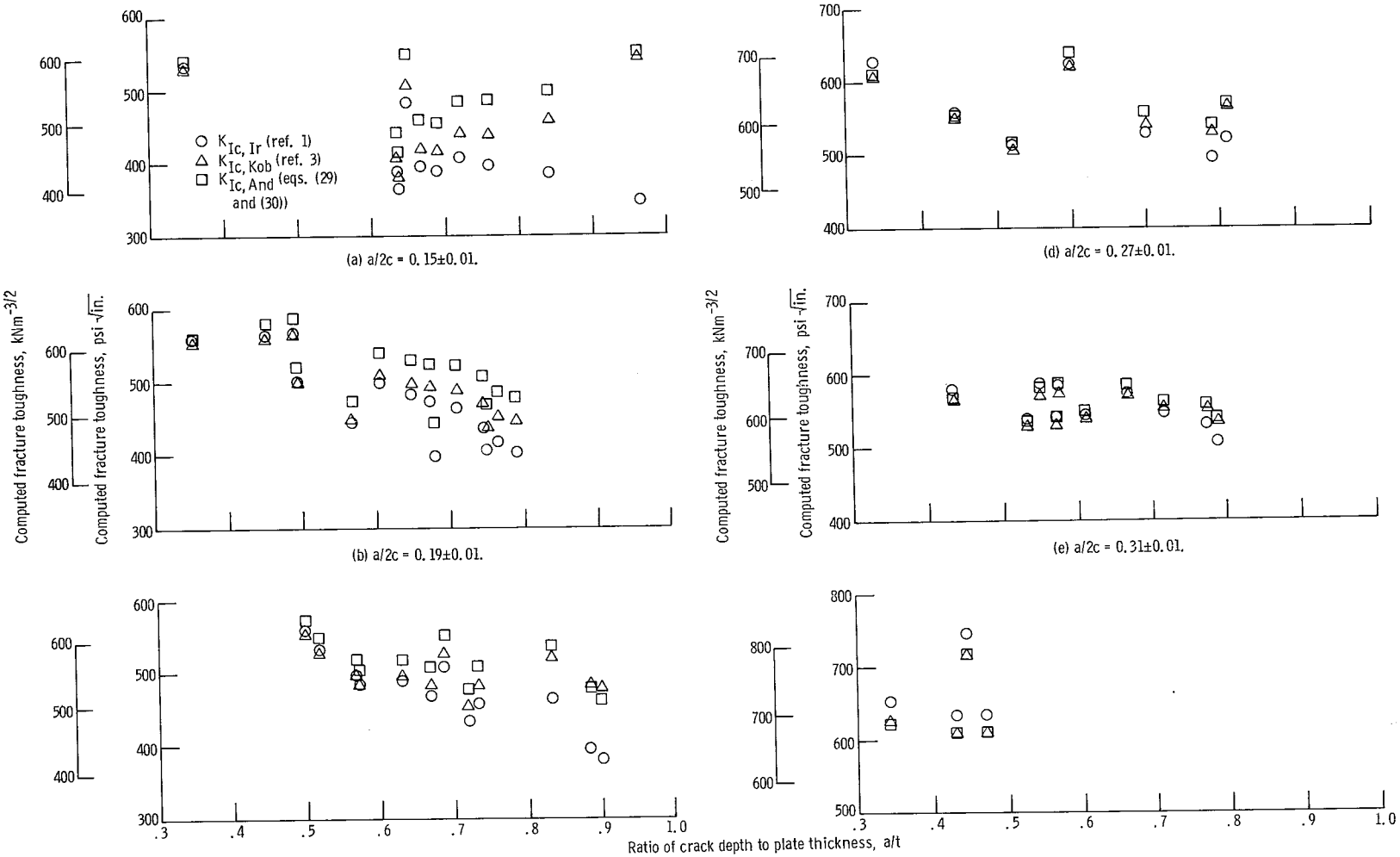

Figure 6. - Computed fracture toughness for epoxy specimens tested in air, for various ratios of crack depth to crack length a/2c. (Data from ref. 8.)

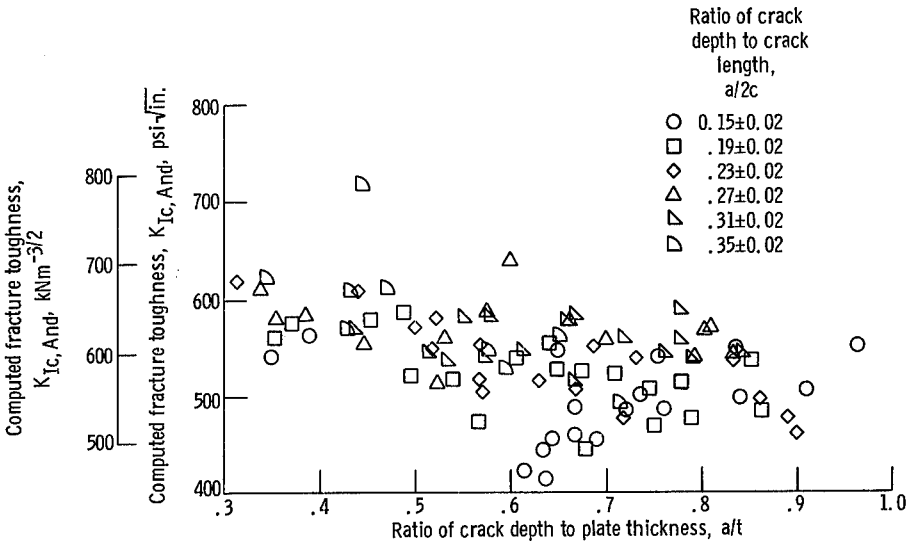

Figure 7. - Computed fracture toughness (eqs. (29) and (30)) for all epoxy specimens, tested in air. (Data from ref. 8.)

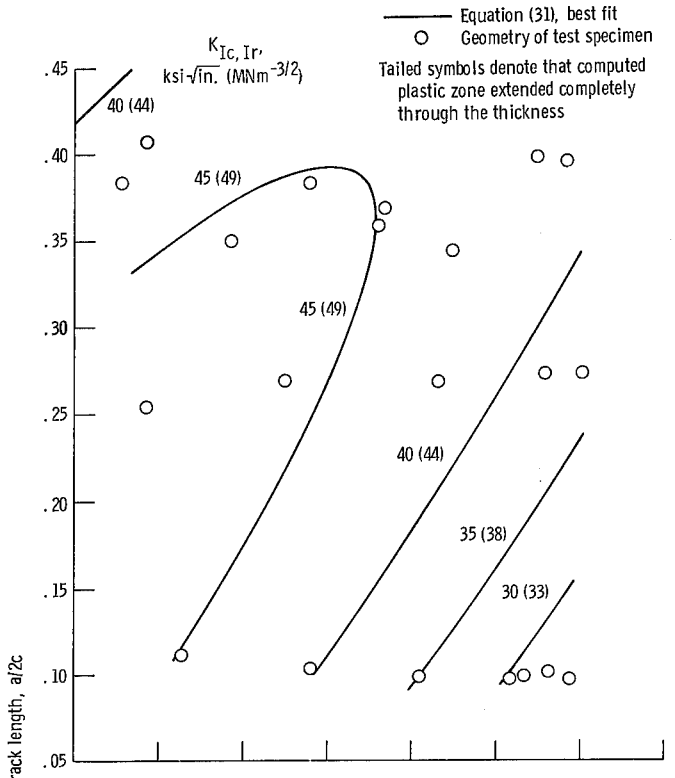

(a) Fracture toughness computed according to reference 1.

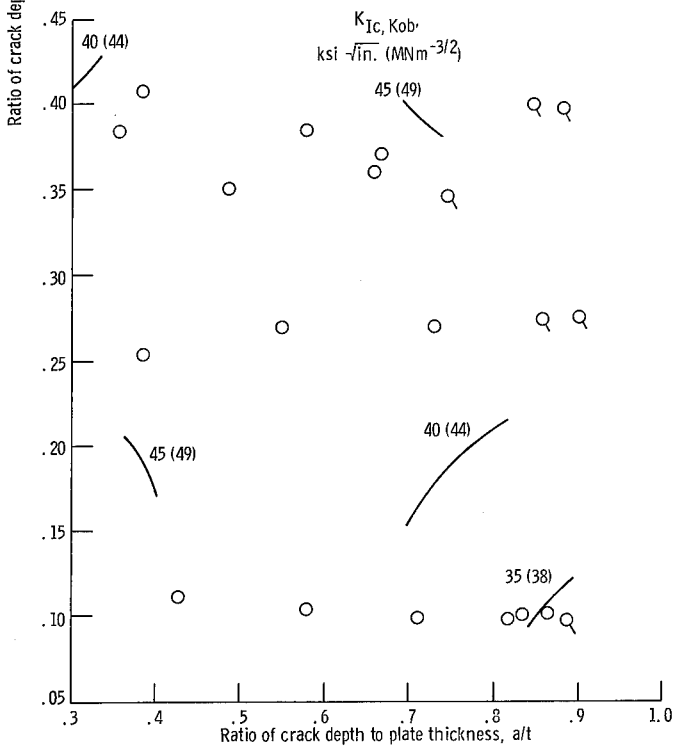

(b) Fracture toughness computed according to reference 3.

Figure 8. - Contour lines of constant computed fracture toughness for 2219-T87 aluminum alloy specimens tested in liquid nitrogen at -320° F (77 K). Crack geometry shown by plotted points.

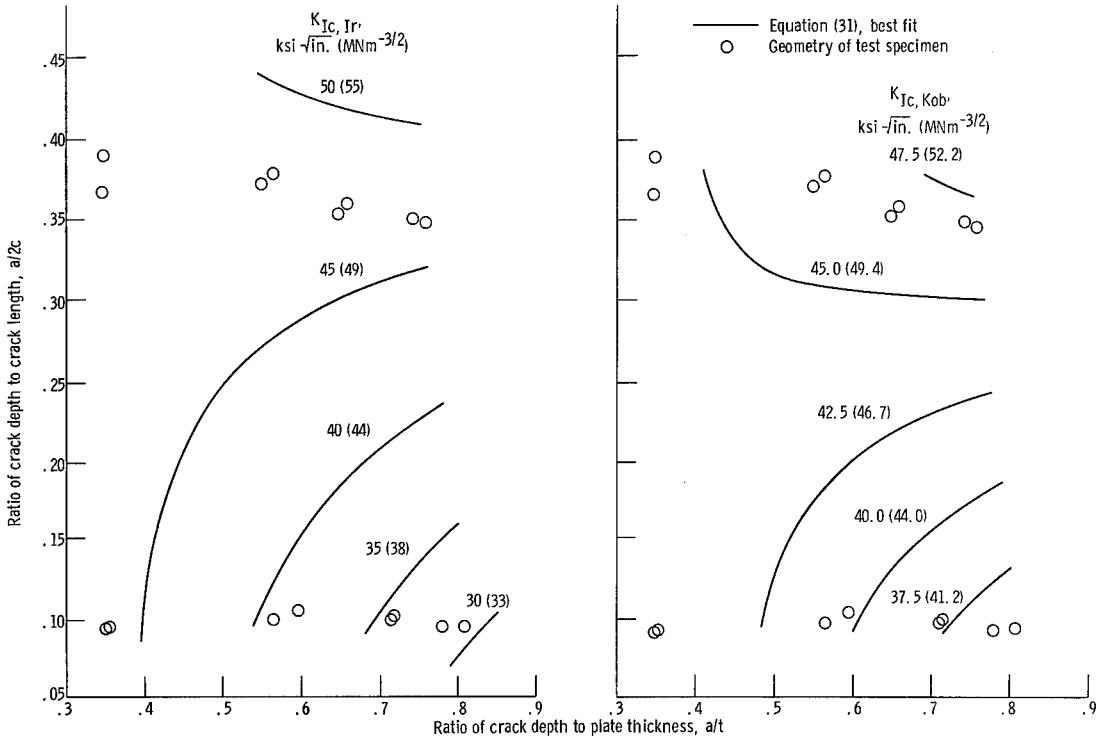

(a) Fracture toughness computed according to reference 1.

(b) Fracture toughness computed according to reference 3.

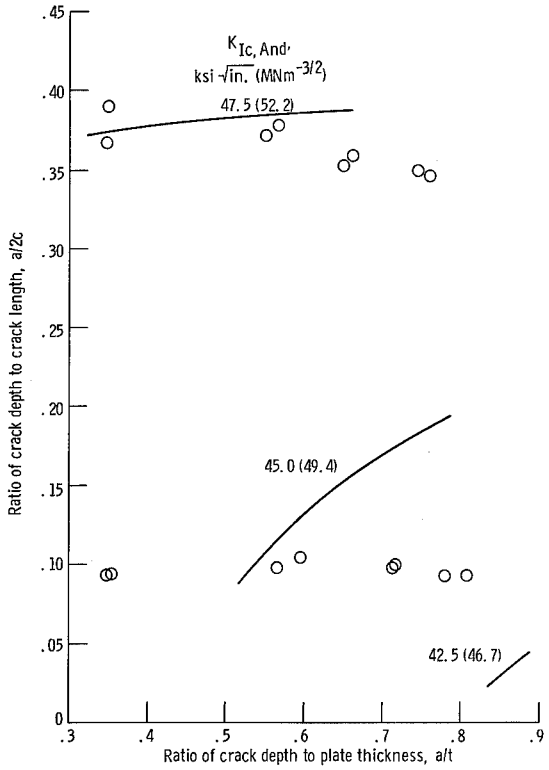

(c) Fracture toughness computed according to this report (eqs. (29) and (30)).

Figure 9. - Contour lines of constant computed fracture toughness for 2219-T87 aluminum alloy specimens tested in liquid hydrogen at -423° F (20 K). Crack geometry shown by plotted points.

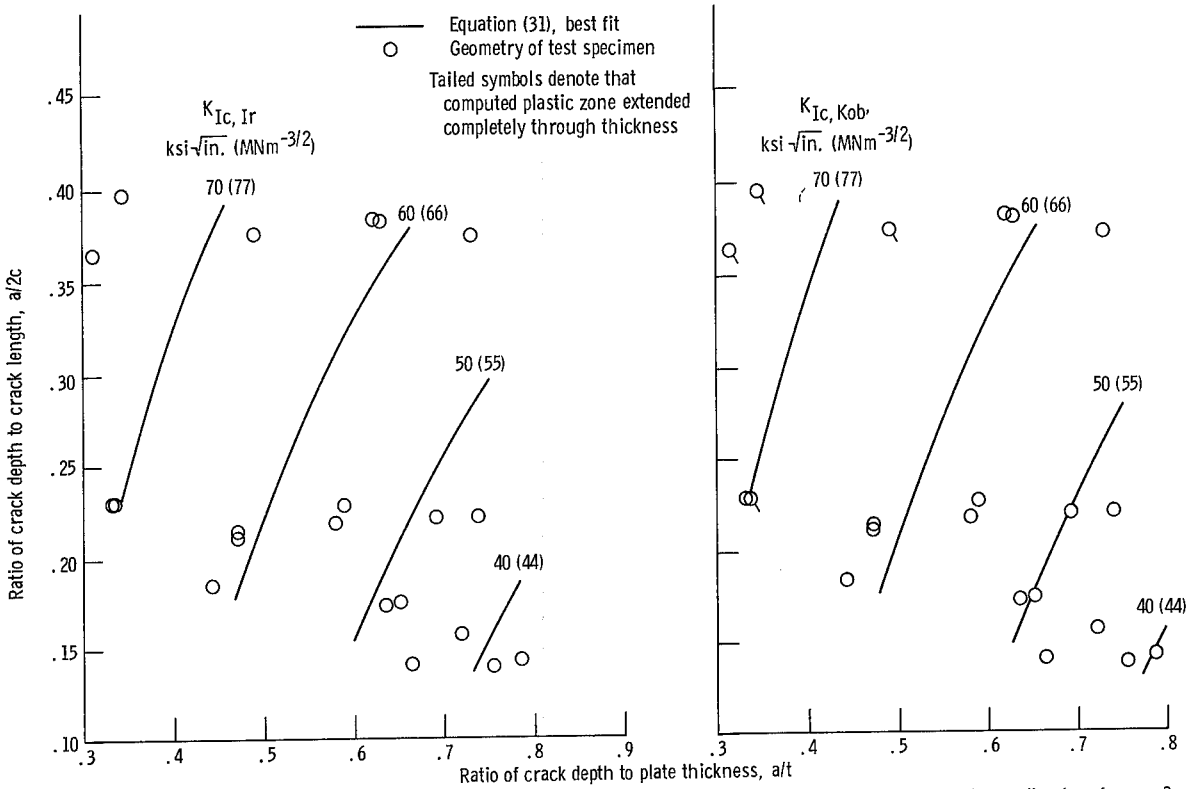

(a) Fracture toughness computed according to reference 1.

(b) Fracture toughness computed according to reference 3.

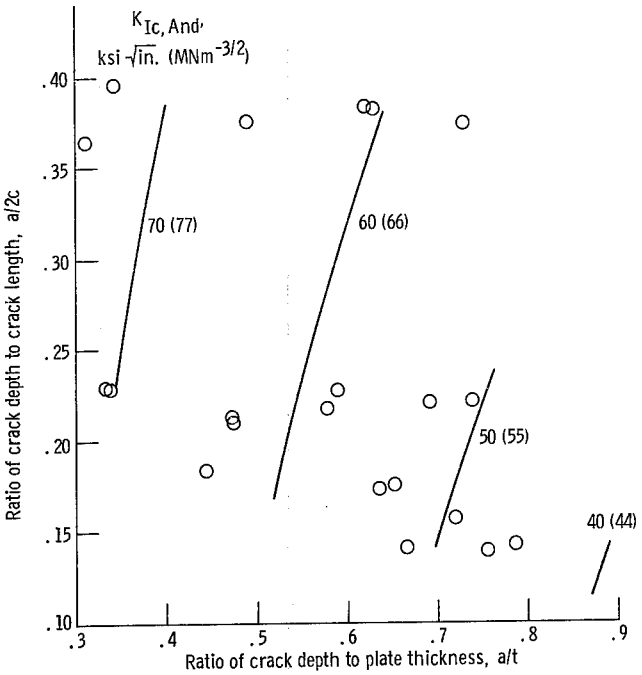

(c) Fracture toughness computed according to this report (eqs. (29) and (30)).

Figure 10. - Contour lines of constant computed fracture toughness for titanium-5Al-2.5Sn-ELI alloy specimens tested in liquid nitrogen at -320° F (77 K). Crack geometry shown by plotted points.

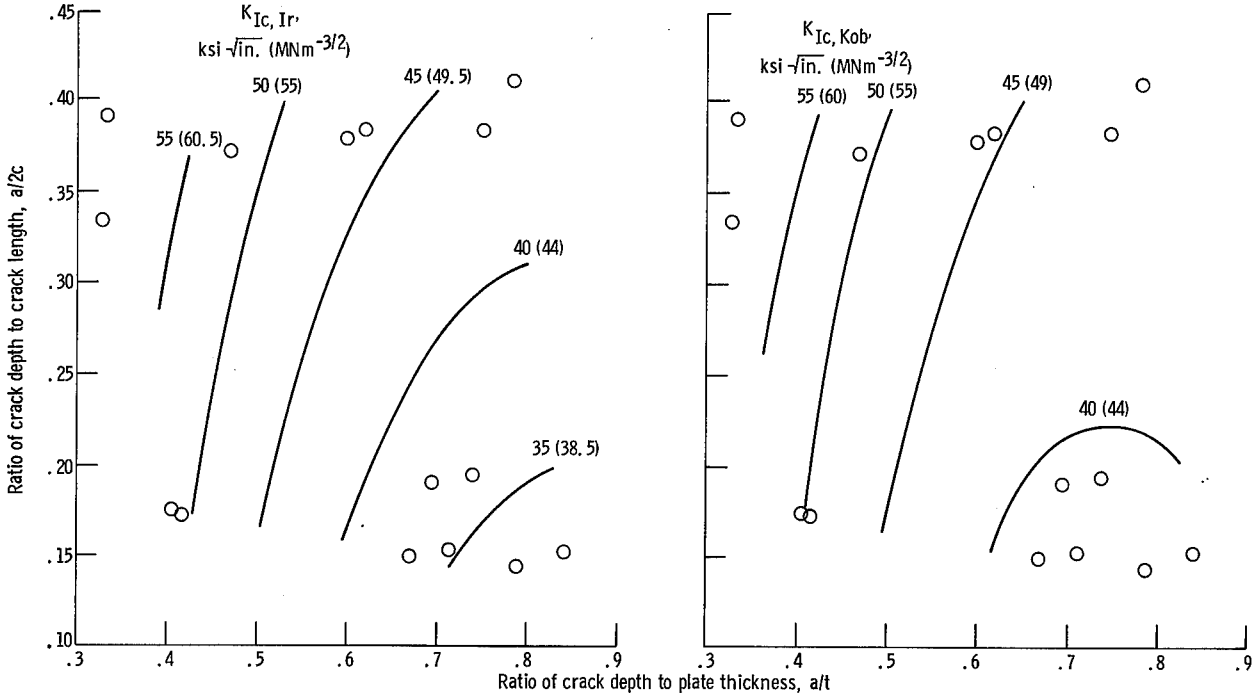

(a) Fracture toughness computed according to reference 1.

(b) Fracture toughness computed according to reference 3.

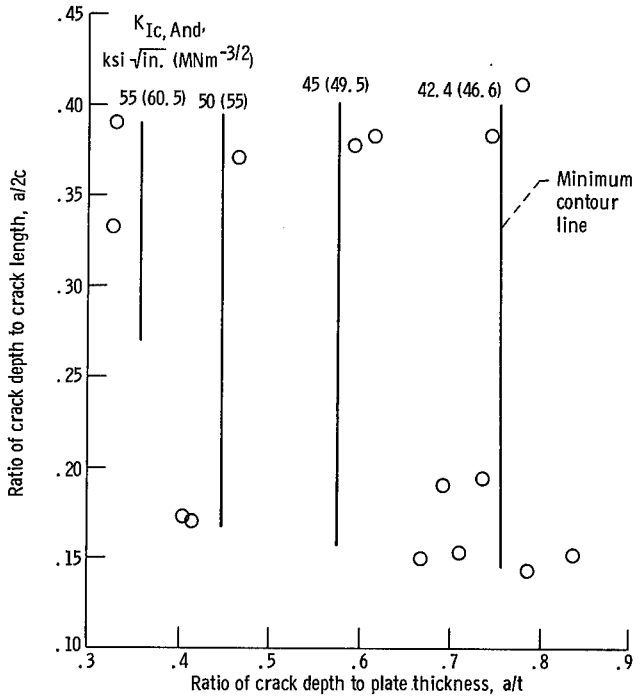

(c) Fracture toughness computed according to this report (eqs. (29) and (30)).

Figure 11. - Contour lines of constant computed fracture toughness for titanium-5Al-2.5Sn-ELI alloy specimens tested in liquid hydrogen at -423° F (20 K). Crack geometry shown by plotted points.

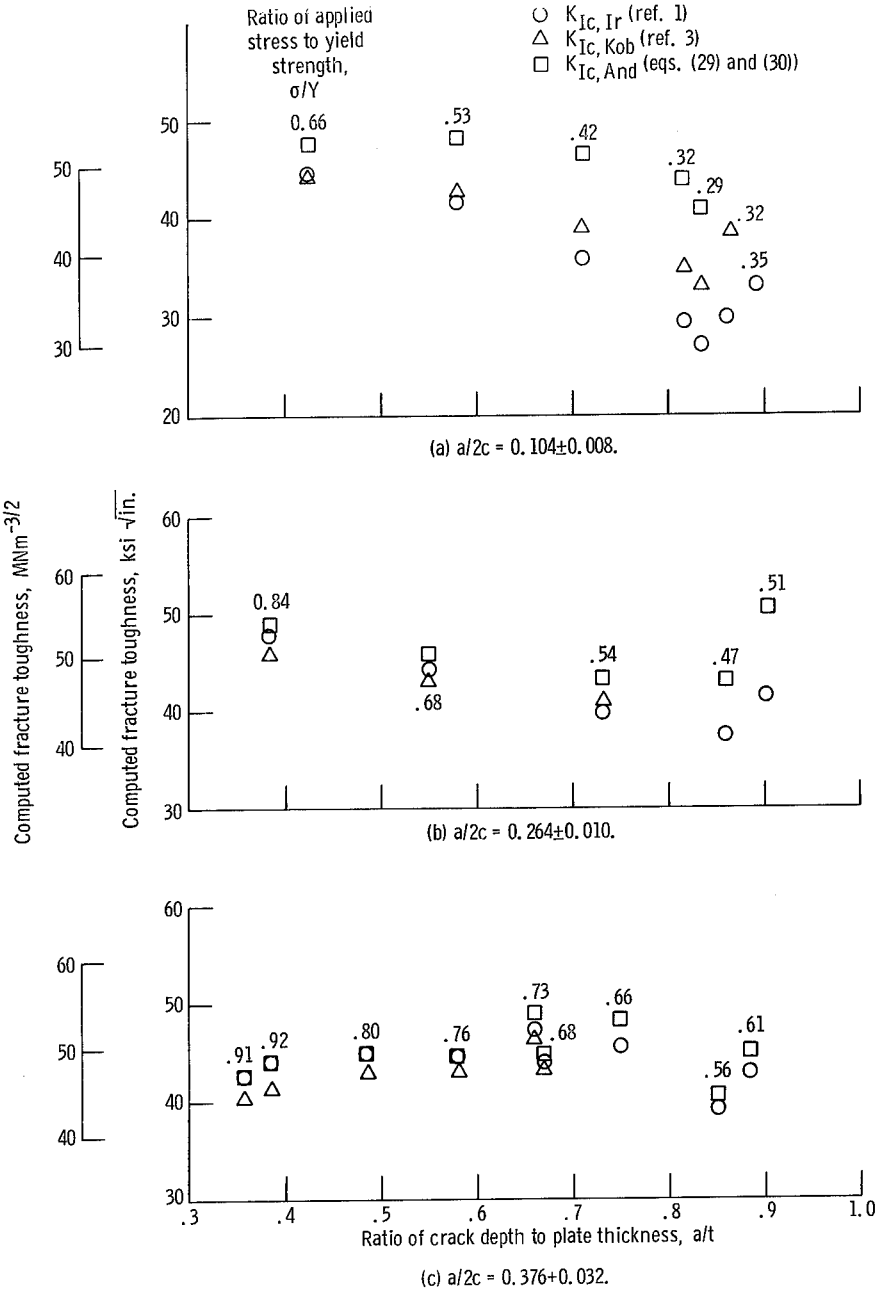

Figure 12. - Computed fracture toughness for 2219-T87 aluminum alloy specimens tested in liquid nitrogen at -320° F (77 K), for various ratios of crack depth to crack length a/2c. (Data from ref. 10.)

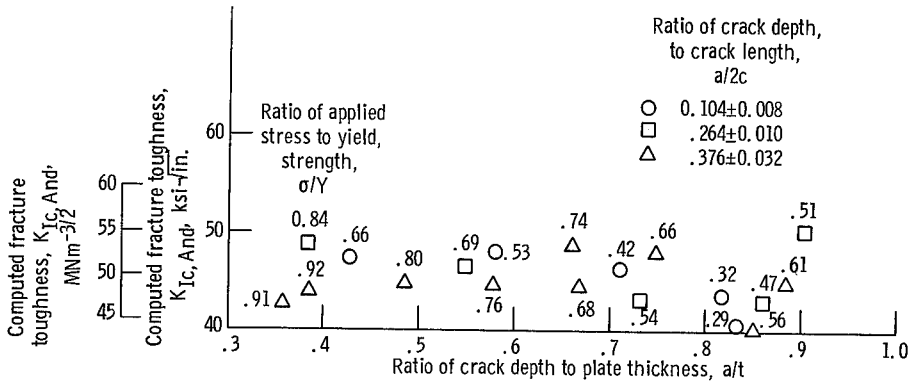

Figure 13. - Computed fracture toughness (eqs. (29) and (30)) for all 2219-T87 aluminum alloy specimens tested in liquid nitrogen at -320° F (77 K). (Data from ref. 10.)

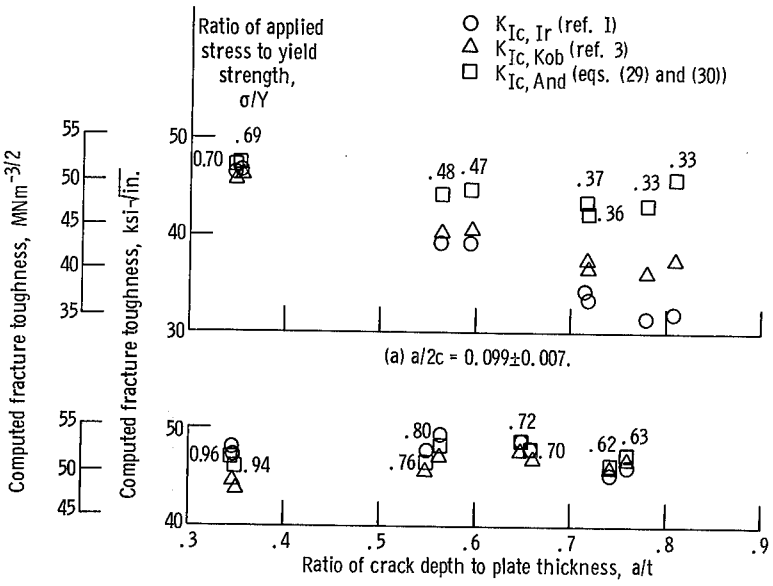

Figure 14. - Computed fracture toughness for 2219-T87 aluminum alloy specimens tested in liquid hydrogen at -423° F (20 K), for two ratios of crack depth to crack length a/2c. (Data from ref. 10.)

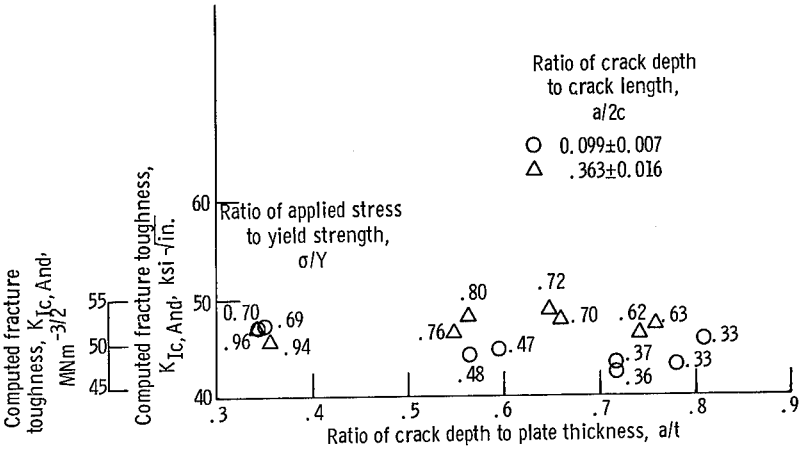

Figure 15. - Computed fracture toughness (eqs. (29) and (30)) for all 2219-T87 aluminum alloy specimens tested in liquid hydrogen at -423° F (20 K). (Data from ref. 10).

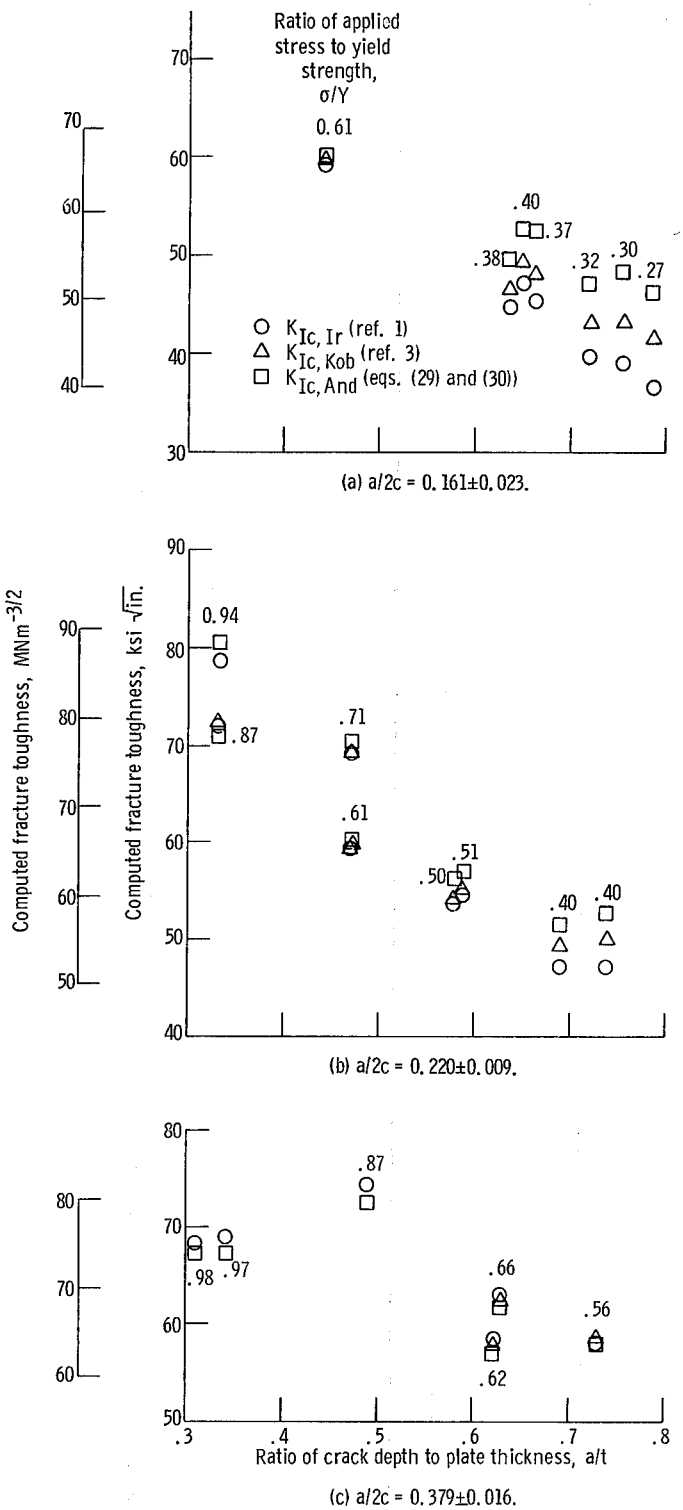

Figure 16. - Computed fracture toughness for titanium-5Al-2.5Sn-ELI alloy specimens tested in liquid nitrogen at -320° F (77 K), for three ratios of crack depth to crack length a/2c. (Data from ref. 10.)

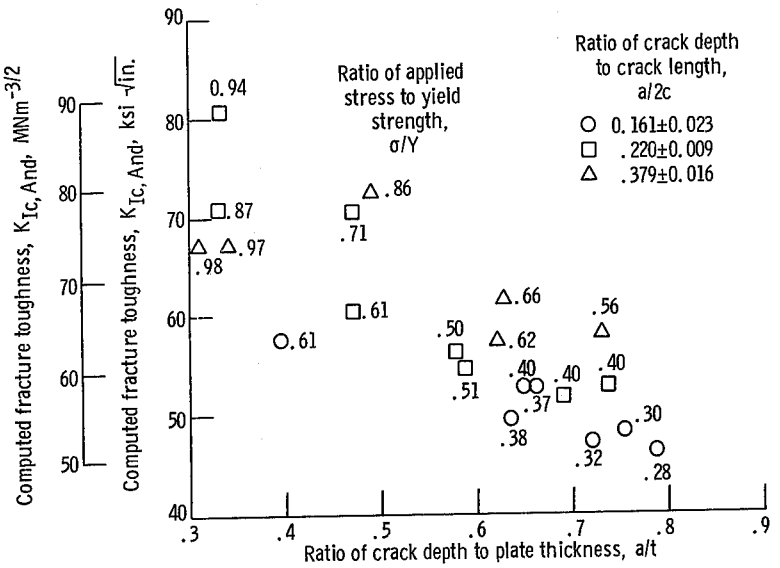

Figure 17. - Computed fracture toughness (eqs. (29) and (30)) for all titanium-5Al-2.5Sn-ELI alloy specimens tested in liquid nitrogen at -320° F (77 K). (Data from ref. 10.)

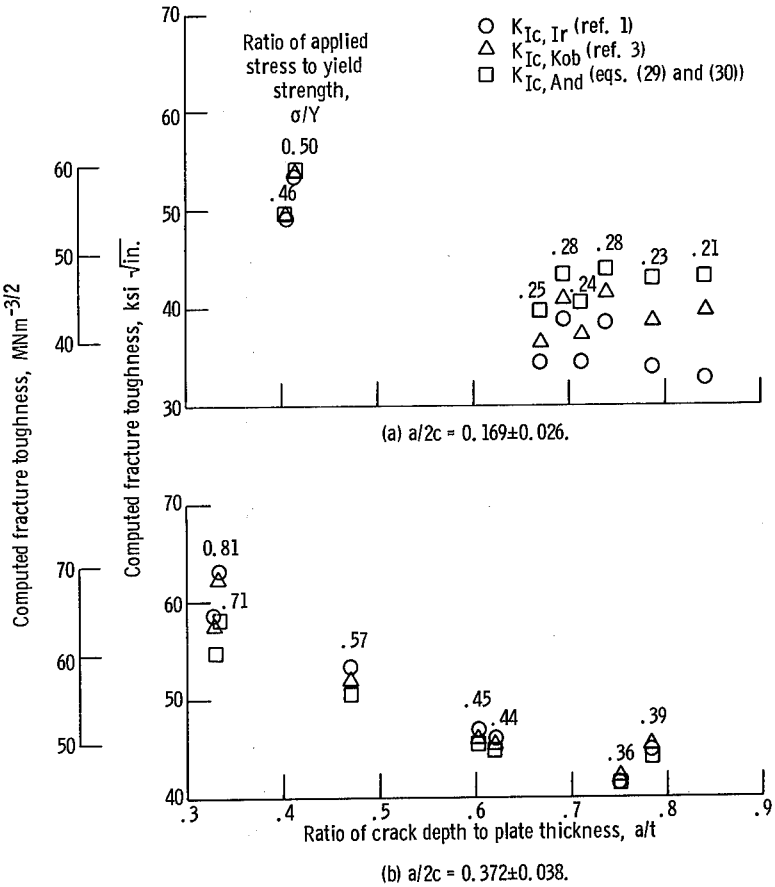

(a) a/2c = 0. 169±0. 026.

(b) a/2c = 0. 372±0. 038.

Figure 18. - Computed fracture toughness for titanium-5Al-2.5Sn-ELI alloy specimens tested in liquid hydrogen at -423° F (20 K), for two ratios of crack depth to crack length a/2c. (Data from ref. 10.)

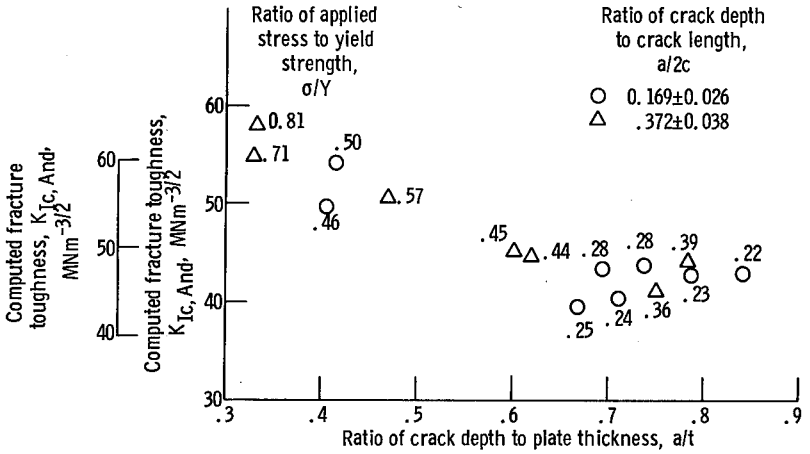

Figure 19. - Computed fracture toughness (eqs. (29) and (30)) for all titanium-5Al-2.5Sn-ELI alloy specimens tested in liquid hydrogen at -423° F (20 K). (Data from ref. 10.)

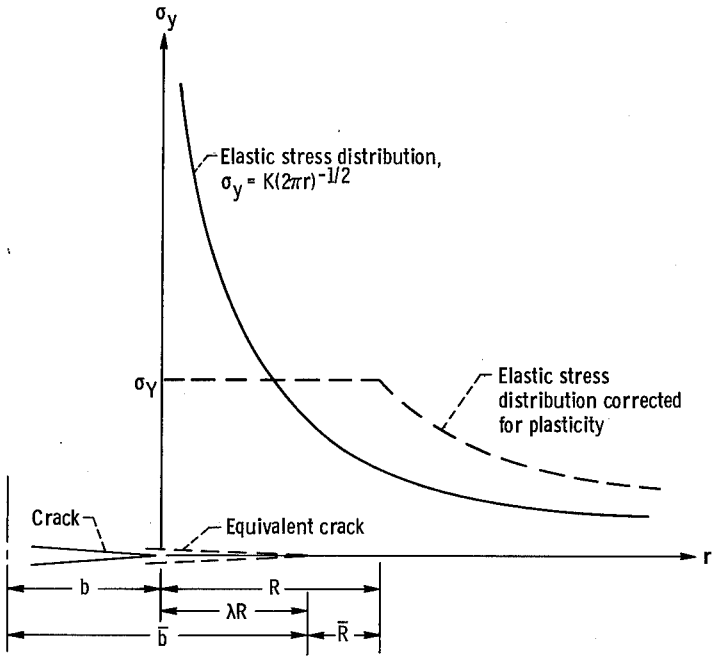

Figure 20. - Stress distribution in presence of plasticity.

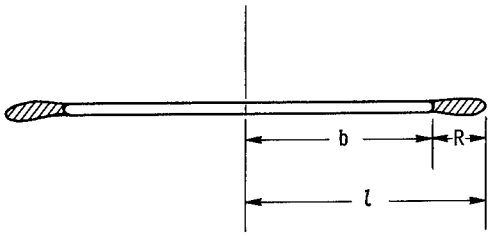

Figure 21. - Plastic zone at crack tip.

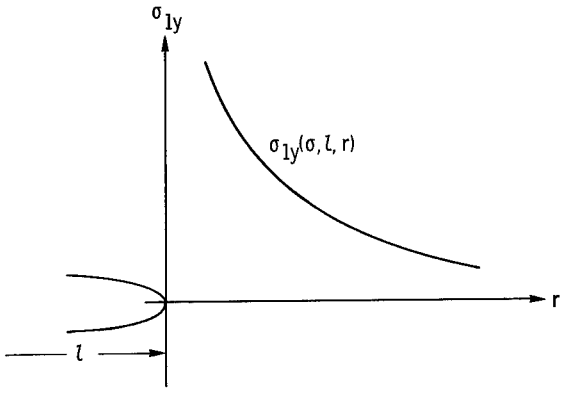

Figure 22. - Stress ahead of virtual crack caused by remote stress.

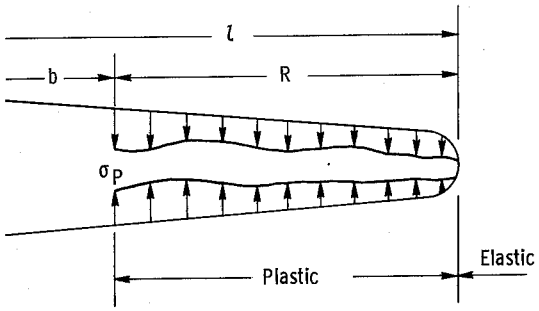

Figure 23. - Constraint of virtual crack border.

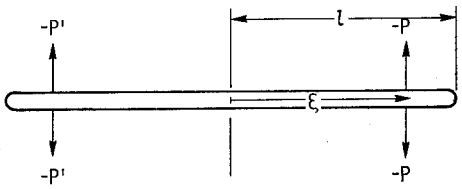

Figure 24. - Negative splitting forces.

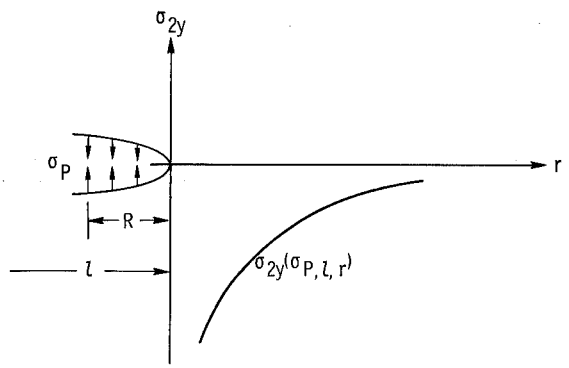

Figure 25. - Stress ahead of virtual crack caused by σ_P.

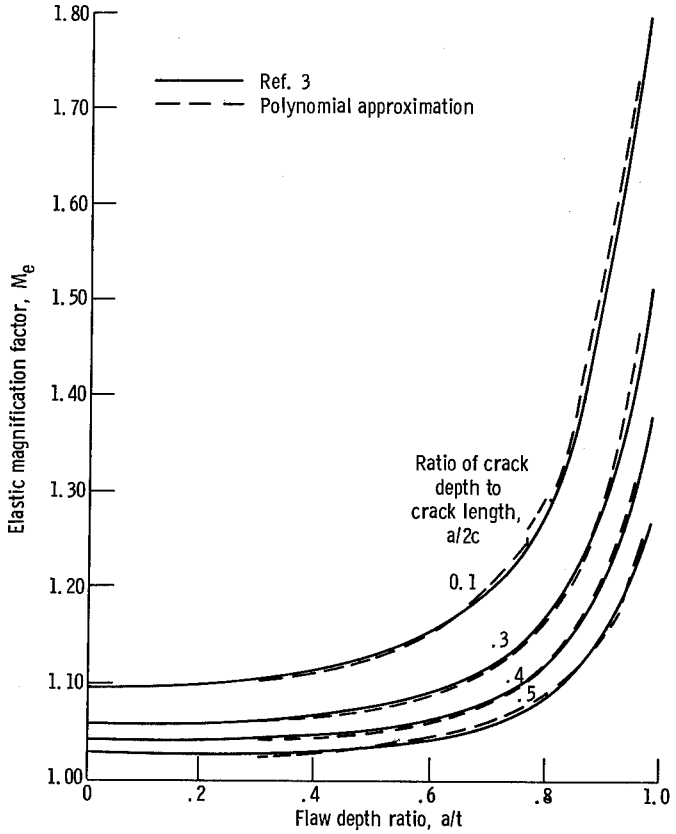

Figure 26. - Polynomial approximation to elastic stress intensity magnification factor of reference 3.

"The aeronautical and space activities of the United States shall be conducted so as to contribute . . . to the expansion of human knowledge of phenomena in the atmosphere and space. The Administration shall provide for the widest practicable and appropriate dissemination of information concerning its activities and the results thereof."

—NATIONAL AERONAUTICS AND SPACE ACT OF 1958

NASA SCIENTIFIC AND TECHNICAL PUBLICATIONS

TECHNICAL REPORTS: Scientific and technical information considered important, complete, and a lasting contribution to existing knowledge.

TECHNICAL NOTES: Information less broad in scope but nevertheless of importance as a contribution to existing knowledge.

TECHNICAL MEMORANDUMS: Information receiving limited distribution because of preliminary data, security classification, or other reasons.

CONTRACTOR REPORTS: Scientific and technical information generated under a NASA contract or grant and considered an important contribution to existing knowledge.

TECHNICAL TRANSLATIONS: Information published in a foreign language considered to merit NASA distribution in English.

SPECIAL PUBLICATIONS: Information derived from or of value to NASA activities. Publications include conference proceedings, monographs, data compilations, handbooks, sourcebooks, and special bibliographies.

TECHNOLOGY UTILIZATION PUBLICATIONS: Information on technology used by NASA that may be of particular interest in commercial and other non-aerospace applications. Publications include Tech Briefs, Technology Utilization Reports and Notes, and Technology Surveys.

Details on the availability of these publications may be obtained from:

SCIENTIFIC AND TECHNICAL INFORMATION DIVISION

NATIONAL AERONAUTICS AND SPACE ADMINISTRATION

Washington, D.C. 20546